2005

# Effects of Finite Amplitude Bottom Topography on Ocean Variability

Dmitri A. Leonov

THE FLORIDA STATE UNIVERSITY

COLLEGE OF ARTS AND SCIENCES

# EFFECTS OF FINITE AMPLITUDE BOTTOM TOPOGRAPHY ON OCEAN VARIABILITY

By

DMITRI A. LEONOV

A Dissertation submitted to the
Department of Oceanography
in partial fulfillment of the
requirements for the degree of
Doctor of Philosophy

Degree Awarded:
Summer Semester, 2005

The members of the Committee approve the dissertation of Dmitri A. Leonov defended on May 31, 2005

William K. Dewar
Professor Directing Thesis

Ionel Michael Navon
Outside Committee Member

Allan J. Clarke
Committee Member

William M. Landing
Committee Member

James C. McWilliams
Committee Member

Doron Nof
Committee Member

Melvin E. Stern
Committee Member

The Office of Graduate Studies has verified and approved the above named committee members.

*моим родителям, жене и дочке Маше*

# ACKNOWLEDGEMENTS

First of all, I would like to thank my major professor, William K. Dewar for his ideas and tremendous support. I am especially grateful to Prof. Melvin E. Stern, who is on my committee, for bringing me to FSU and exposing me to the high standard of research on his team. I would also like to thank other members of my committee for their knowledge and support throughout my studies in the program and valuable comments on the dissertation: Professors A. J. Clarke, W. M. Landing, J. C. McWilliams, I. M. Navon and Doron Nof. Interesting conversations with Prof. James C. McWilliams and his team during my visits to UCLA are especially recognized.

# TABLE OF CONTENTS

# LIST OF TABLES

# LIST OF FIGURES

# ABSTRACT

The wind-driven oceanic circulation in the presence of bottom topography that isopycnals intersect is examined in an idealized setting. A modified quasi-geostrophic (QG) model has been designed and implemented. The model allows staircase bottom topography: topographic breaks decompose the lateral domain into subdomains consisting of fixed numbers of layers. Topographic shelves are placed within small (order Rossby number) vertical distances from the undisturbed layer interfaces. Each shelf can have topographic variations of the same scale. An elliptic solver inverting potential vorticity into geostrophic streamfunctions was designed based on the Capacitance matrix method. Solutions are matched at the topographic breaks by adding fictitious potential vorticity sources.

The model has been tested against the problem of trapped topographic waves over a cliff. The results obtained for small-steepness disturbances agree with a weakly non-linear theory developed by Dewar and Leonov. Steeper disturbances break in a way that favors onshelf eddy detachment and transport of undiluted properties onto the shelf. The model has been further applied to the basin-scale wind-driven circulation problem in a 3-layer configuration with a continental shelf in the western part of the domain. Double-gyre wind forcing has been considered.

The topographic shelves are responsible for dynamics absent in classical idealized eddy-resolving QG models which have been the preferred numerical tool for the study of low frequency intrinsic ocean variability. The top-layer flow interacts with the shelf topography by means of vortex tube stretching and vorticity dissipation due to bottom drag. This mechanism reduces the role of horizontal friction as a controlling factor in the dynamics. The results obtained for different parameter regimes (free-slip, no-slip boundary condition, different values of the viscosity) show reduced sensitivity to the type of dynamic boundary condition, compared to classical results.

The intrinsic variability of the flow is affected by the new mechanism of on- and offshelf transport of potential vorticity. The role of horizontal friction is again reduced, as shown by

the modeling results. Spatiotemporal patterns of the variability have been analyzed. Most of the patterns are insensitive to the type of boundary condition (free-slip vs. no-slip), and qualitatively resemble classical no-slip results.

# CHAPTER 1

# INTRODUCTION

## 1.1 Motivation

The study of ocean variability and what influences it is part of a larger problem: understanding coupled climate variability. The North Atlantic Oscillation (NAO) is an atmospheric signal possibly exhibiting a preferred decadal timescale [13]. The length of the recorded signal is only about 130 years, so the observed enhanced power at the decadal frequency band is not pronounced enough to be statistically significant [36] leaving it uncertain if there is a physical mechanism behind this peak [18]. If in fact such a physical process exists, understanding it might allow some degree of predictability at the decadal time scale, and, possibly, some ability to distinguish between natural and anthropogenic components of climate change. Demonstrating even a small degree of predictability to the climate would be an important result.

The length of the observational record will not increase significantly in the near future. The study of climate has thus moved ahead using climate models, many of which exhibit some consistency with observations. Important candidates for modes of variability involve ocean modes: both intrinsic and forced. Unlike the atmosphere, the ocean can exhibit its own distinguished decadal time scales, some of which may be associated with wave dynamics (basin modes), and some with mesoscale eddies. So examining how the ocean behaves on its own is a reasonable first step towards understanding coupled climate variability.

## 1.2 Wavelike variability

Some studies seek to characterize the large-scale wavelike response in an ocean basin under wind forcing ([15] and references therein). The importance of Rossby waves in

establishing the westward-intensified wind-driven ocean circulation has been well known. In an ocean of constant depth long waves are efficient at carrying energy to the west whereas eastward-propagating short waves are more easily damped by friction. In reality this mechanism is modified by the presence of bottom topography.

*Rhines* [29] analytically examined reflection of low-frequency Rossby waves by abrupt topography in a homogeneous ocean. He used linearized shallow-water equations and demonstrated that a confined slope acts as a potential well which sometimes prevents the waves from escaping the region of the topography. The fundamental mode of trapped variability consists of sinuous lateral displacements of fluid in the cross-slope direction. Its phase propagates pseudo-westward (to the left facing the shallow region), the group speed has the opposite direction and vanishes in the limit of a step topography. A step of finite width allows for higher modes where displacements are not sinuous.

Some analytical studies of trapped topographic waves include stratification. *Rhines* (1970) examined waves in a continuously stratified fluid over a sloping bottom, and studied their linear properties. The use of a homogeneous fluid model was justified for long waves over weak slopes [30]. If the cross-slope fractional depth change is small, quasigeostrophic (QG) potential vorticity equations [21] are applicable. They can be viewed as an approximation to the shallow water equations that allows (weak) vortex tube stretching and at the same time filters out gravity waves.

More recent studies have moved the QG approach into regimes involving *finite amplitude topography* (or finite topography), i.e. bottom topography intersected by isopycnals. Mysak et al. [20] studied the linear stability of coastal currents using a QG model consisting of a one-layer (shelf) and a two-layer (open ocean) parts connected at the shelf break. Thompson [34] allowed finite topography in the framework of QG and used a modified contour dynamics method, where artificial sources of potential vorticity (PV) were added at the topographic breaks to obtain uniformly valid solutions. *Pedlosky* [22] studied transmission of Rossby waves past topographic barriers using a QG approximation. Narrow gaps were allowed in thin meridional barriers which otherwise divided the two-layer basin into sub-basins. The finite topography case was considered when the gaps connected only the upper layer. Surprisingly, such barriers turned out to be quite inefficient at blocking waves.

Dewar and Leonov [6] examined wave evolution of lateral disturbances over abrupt and confined topography. Weak and finite topography cases were considered. The problem was addressed analytically on an infinite, inviscid QG f-plane with step topography. A formal exact solution, similar to the one used by Thompson in [34], was approximated analytically in the limit of small steepness of the disturbance, and the weakly-nonlinear properties of the waves were discussed.

In this thesis a numerical grid-point QG model allowing finite topography is implemented. The model connects to the Dewar and Leonov study [6] by validation through comparison with the known solutions and through extension of the wave behavior to finite amplitude.

## 1.3 Wind-driven circulation

There is considerable observational evidence of an energetic low-frequency (annual to interannual and beyond) variability in some regions of the World Ocean (see for example [35]). Recent observational studies have shown that in some parts of the ocean the eddy kinetic energy (EKE) varies significantly on interannual time scales (see [23] and references therein), the reasons for which remain unclear. Primitive equation models which give realistic time-mean behavior are very expensive to run at the high resolutions required for proper representation of eddy variability [3]. Thus with present computing power it is not feasible to use primitive equation models to obtain statistically significant statements about intrinsic ocean variability.

Focusing on variability on time scales of months to decades allows for some idealizations, e.g. gravitational equilibrium (which filters out fast gravity waves) and the neglect of diabatic effects (associated with overturning circulation variability on centennial time scales). The resulting idealized equations can be run at eddy resolutions for the needed duration. The quasigeostrophic approximation is thus recommended as a suitable approximate equation set for the study of such variability. A pioneering study was done in 1978 by Holland [12], who showed that a quasigeostrophic (QG) ocean model subject to a steady wind forcing generates broad band internal variability.

Berloff and McWilliams [2] used a QG model to investigate the onset of variability (as Reynolds number increases) and categorize its modes. Problem parameters were varied (symmetric or asymmetric wind forcing, 1.5 or 2 layer stratification). In each case regimes of

circulation under steady forcing were explored for a wide range of Reynolds numbers ($Re$). The regimes included steady circulation, periodic and quasi-periodic fluctuations and chaotic circulation characterized by a broadband spectrum. Spatiotemporal patterns were analyzed with an EOF decomposition combined with time filtering.

Some studies look into low-frequency instabilities near the beginning of the bifurcation tree, i.e. periodic and quasi-periodic fluctuations at relatively low $Re$. Simonnet and Dijkstra [32] found such instabilities to be robust over a hierarchy of models. Whether these instabilities will manifest themselves in fully turbulent regime is still an open question. Further studies using idealized eddy-resolving models are currently being conducted to resolve the issue. Quasigeostrophy continues to be the main computational tool in the studies of intrinsic ocean variability at annual to decadal time scales. Some recent applications of QG are aimed at analyzing ocean response to periodic and stochastic wind forcing [5] and studying coupled climate variability ([10], [14]).

In 1992 Haidvogel et al. [7] pointed out a significant drawback of QG modeling. They showed that the model results depend significantly on a boundary condition coefficient the value of which is not strongly constrained by physical reasoning. Vertical walls, where the boundary condition applies, represent an idealization of topographic slopes and shelves, which are examples of finite topography.

Hallberg and Rhines [8] explored a fundamental effect of finite topography on geophysical flows. Using a density coordinate primitive equation ocean model, they showed that finite topography provides a source of high PV for the large scale circulation: in short, the positive rest-state PV over the topography is swept off by the circulation and transformed into relative vorticity. In the simulations presented in [8] the influence of finite topography on the circulation was of equal importance to the effect of eddy stirring and homogenization of PV in the subsurface interior. Fluid pushed onto the slopes and shelves interacts frictionally with the bottom. It should be noted that virtually all frictional encounters of the real ocean with topography occurs by means of bottom boundary layers.

QG equations for a continuously stratified fluid consider the vertical velocity as a small (order Rossby number) perturbation to the horizontally non-divergent geostrophic flow. Therefore only small variations of the bottom topography are allowed. Mathematically they are specified in the bottom boundary conditions at a fixed depth. Thus, in the

vertically-discretized equations only the lowest layer can interact with the bottom by means of the topographic beta-effect and bottom drag.

The modified QG approach used in this thesis allows more fluid to interact with the bottom topography without violating the scaling assumptions behind the QG theory. One starts with the layer (vertically-discretized) equations. Topographic breaks decompose the lateral domain into regions which consist of fixed numbers of active layers. Topographic shelves are placed within small (of order Rossby number) vertical distances from the undisturbed layer interfaces. Each shelf can have topographic variations of the same scale, as in classic QG theory. In this way, near-surface densities interact with topography by means of bottom boundary layers. This process is more physically consistent with the real ocean than is interaction with frictional vertical walls in classical QG. In this thesis, such finite-topography models are used to compute the classical wind-driven circulation and to comment on the resulting mean states and intrinsic variability.

## 1.4 Dissertation outline

The modified QG numerical model is formulated in Chapter 2. Chapter 3 focuses on results of a channel implementation of the model and examines trapped topographic waves. The weakly non-linear equation in [6] is shown to be incomplete, having missed one quadratic contribution. A corrected equation is derived and compared to two-dimensional calculations using the modified QG model. This calculation acts as a test on the new numerical technique. Strong-steepness regimes are then considered. The onshelf−offshelf asymmetry in the wave breaking results in a preferred onshelf transport mechanism by eddy detachment.

In Chapter 4 the finite-topography QG model is applied to the wind-driven circulation problem. In a series of experiments, the modified and standard QG models were run with similar parameters chosen to qualitatively represent the extra-tropical North Atlantic. The numerical results are analyzed to test the hypothesis that introducing finite topography in the model makes it less sensitive to the lateral boundary conditions. Variability in the finite-topography model is also examined in order to find patterns robust over different parameter regimes (types of lateral boundary conditions). These results demonstrate the effect finite amplitude topography has on the mean structure and intrinsic low frequency variability

of the wind-driven circulation. Chapter 5 summarizes the results, draws conclusions and discusses possible implications.

# CHAPTER 2

# THE MODEL

The purpose of this chapter is to outline the theoretical development of the modified QG model and to discuss its numerical implementation.

## 2.1 Domain geometry and consistency check

The following notation from the set theory will be applied here to domains on the plane as well as discretized domains (sets of gridnodes on a 2D grid):

| | |
|---|---|
| $A \subset B$ | $A$ is a subset of $B$ (all elements of A are in B) |
| $A \backslash B$ | $A$ minus $B$: set of all elements of $A$ that are not in $B$ |

If $A \subset B$, we have $B = A + B \backslash A$, where + means addition of two non-intersecting subsets.

We consider a stepwise geometry: the fluid in corresponding layers occupies nested domains $\mathrm{D}_k$ $(k = 1, ...N)$:

$$\mathrm{D}_N \subset \ldots \mathrm{D}_2 \subset \mathrm{D}_1, \quad \mathrm{D}_1 \text{ is a connected domain.}$$

A possible configuration of bottom topography is shown in Fig. 2.1 (vertical cross-section) and 2.2 (view from the top). The area $\mathrm{D}_k \backslash \mathrm{D}_{k+1}$ is a topographic shelf (or top of a seamount) where $k^{\text{th}}$ layer contacts the bottom. Vertically the topographic shelves are placed within small (order Rossby number) distances from the undisturbed layer interfaces. Each shelf can have topographic variations of the same scale, as in classic QG theory. For such basin geometry a quasigeostrophic (QG) ocean model is developed.

Steep slopes intersected by isopycnals are thus modeled here as abrupt steps. Classical Ekman boundary layer is assumed above the nearly flat shelf topography. In reality though, the Ekman spin-down mechanism becomes nonlinear in the presence of finite topography. As was shown by MacCready and Rhines [17], the buoyant forces shut down the bottom

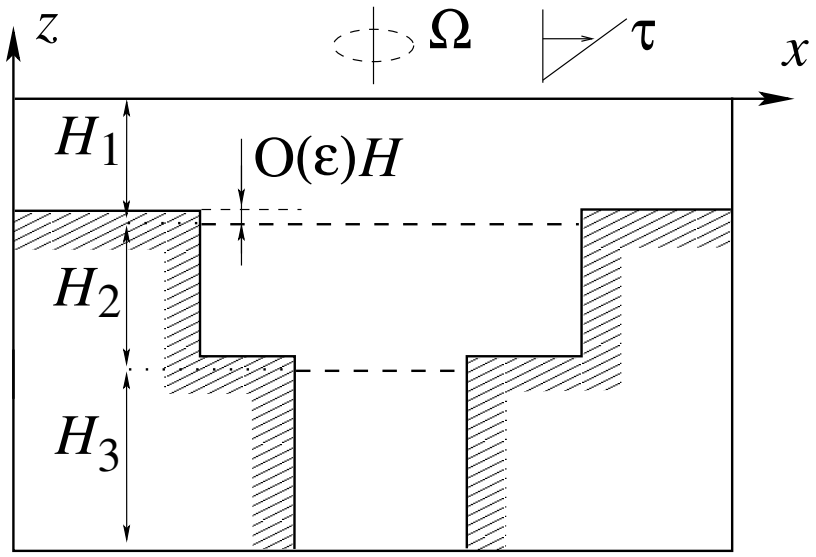


**Figure 2.1**. An example of possible domain geometry

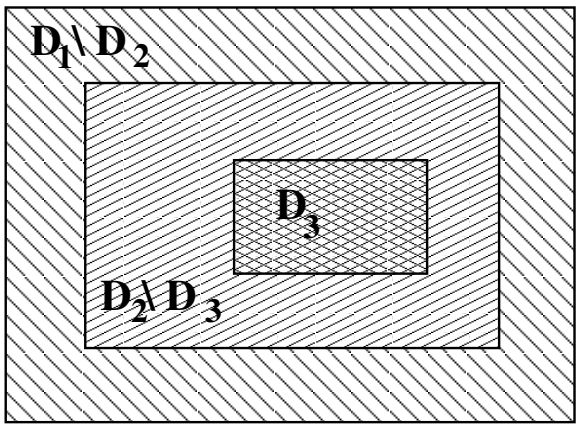


**Figure 2.2**. Domain geometry (view from the top). Areas where each layer contacts topography are shown.

Ekman layer over sloped topography. (See also [16].) If shut down time scale is comparable to the time scale of the mesoscale, the eddies will still feel significant bottom drag; in this work we assume this is true.

The general evolution of such a model will necessarily involve instances where modulations in the interfaces will elevate them above the depth of the shelf break (see Fig. 2.3). Dense fluid will invade the shelf region in a thin layer in which the QG approximations will be invalid. A first consideration in QG model development then involves the evolution of the interface between layers in such an occurrence. We argue here that the penetration of dense fluid onto the shelf is strongly confined and thus in QG theory may be neglected. To show this, consider the problem of the geostrophic adjustment on an f plane of the initial state shown in Fig. 2.3. Let $H_1$, $H_2$ be the layer depths, $g' = g\Delta\rho/\rho_\star$, reduced gravity and $f_0$, the Coriolis parameter. The fluid at the initial state is at rest. We use primitive equation shallow water dynamics and assume that a one-dimensional steady (and thus geostrophic) adjusted state will be reached after disturbances radiate away. Potential vorticity conservation gives in the final steady state

for $x > 0$:

$$\frac{f_0^2}{H_1 - h} = \frac{f_0^2 + p_{1xx}}{H_1 - \eta}, \tag{2.1}$$

$$\frac{f_0^2}{H_2 + h} = \frac{f_0^2 + p_{2xx}}{H_2 + \eta}, \tag{2.2}$$

for $x < 0$:

$$\frac{f_0^2}{H_1} = \frac{f_0^2 + p_{1xx}}{H_1 - \eta}, \tag{2.3}$$

$$\frac{f_0}{H_2 + h} = \frac{f_0 + p_{2xx}}{\eta}, \tag{2.4}$$

where $p_1$, $p_2$ are pressures in the adjusted state and $\eta(x)$ is the interface height relative to the shelf. (We neglect small horizontal fluid displacements in both layers.)

From the hydrostatic balance

$$\eta = h + \frac{p_2 - p_1}{g'}. \tag{2.5}$$

Substituting for $p_1 - p_2$, we get in the approximation $h \ll H_1, H_2$:

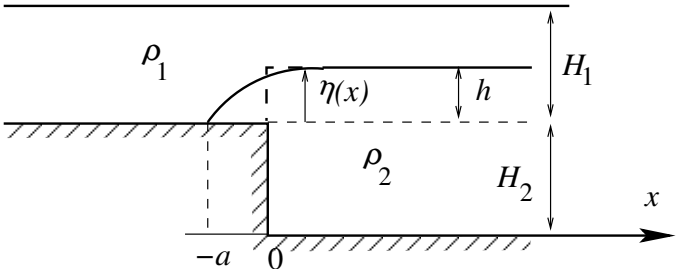


**Figure 2.3**. Geostrophic adjustment problem in presence of topography ($\partial/\partial y = 0$, interface at initial state is shown by thick dashed line)

$$\eta = \begin{cases} h - Ae^{-x/R}, & x > 0, \\ h - Ae^{-x/R} - \frac{f_0^2 x^2}{2g'}, & x < 0 \end{cases} \tag{2.6}$$

Here $R$ is the deformation radius: $R^{-2} = (f_0^2/g')(1/H_1 + 1/H_2)$, and $A$ is a constant which can be found from mass conservation ($0 < A < h$). Noting that for $x < 0$, $\eta < h - f_0^2 x^2/2g'$, we can estimate the fluid penetration distance $a$ (see Fig 2.3):

$$a < \frac{\sqrt{2g'h}}{f_0}, \tag{2.7}$$

So $a \sim R\sqrt{\varepsilon}$ (where $h/H_1 \sim \varepsilon$) and vanishes as $\varepsilon \to 0$. In a perturbative approach based on $\varepsilon$ like the one used to derive QG equations, this is consistently represented by applying a no normal flow boundary condition for the lower layer at $x = 0$ and the requirement of finite PV (smooth streamfunction) in the upper layer.

## 2.2 Mathematical model formulation

Quasigeostrophic (QG) equations are applied to a basin with the geometry described above. Let $n = n(x, y)$ be the number of active layers and $l_k(x, y)$ denote 2-valued functions defined as:

$$l_k(x, y) = \begin{cases} 1 & \text{for } k \geq n, \\ 1 & \text{in } \mathrm{D}_k \backslash \mathrm{D}_{k+1} \text{ (over topography)}, \quad k < n, \\ 0 & \text{in } \mathrm{D}_{k+1} \text{ (over free interface)}, \quad k < n \end{cases}$$

Then the equations for each layer, $k$, of an $N$ layer beta plane model can be written:

$$\left(\frac{\partial}{\partial t}+\mathrm{J}(\psi_k,\cdot)\right)q_k=\delta_{k,1}\frac{f_0}{H_1}w_e+A_H\nabla^4\psi_k-\nabla\cdot(l_k\gamma_k\nabla\psi_k),\quad k=1,\ldots,N \tag{2.8}$$

Here $\psi_k$, $q_k$ are the $k^{\text{th}}$ layer's streamfunction and potential vorticity ($u_k=-\partial_y\psi_k$, $v_k=\partial_x\psi_k$), and J denotes the Jacobian operator $\mathrm{J}(p,q)=\partial_x p\,\partial_y q-\partial_x q\,\partial_y p$. Quasigeostrophic potential vorticity $q_k$ is defined as

$$q_k=\nabla^2\psi_k-\frac{f_0^2}{g'_{k-1}H_k}\left(\psi_k-\psi_{k-1}\right)-\frac{(1-l_k)f_0^2}{g'_kH_k}\left(\psi_k-\psi_{k+1}\right)+\beta y+l_kf_0\frac{h_b}{H_k}. \tag{2.9}$$

Here $\nabla=\{\partial_x,\partial_y\}$, $w_e=\nabla\times\boldsymbol{\tau}/\rho f_0$ is the Ekman pumping velocity, $\boldsymbol{\tau}=\{\tau^{(x)},\tau^{(y)}\}$ is the wind stress, $A_H$ is the horizontal eddy viscosity, $\gamma_k$ is the bottom drag coefficient for the $k^{\text{th}}$ layer; $g'_k=g(\rho_{k+1}-\rho_k)/\rho_\star$ are reduced gravities ($g'_0=g'_N=\infty$), and $H_k$ are undisturbed layer thicknesses.

At the lateral boundaries $\partial\mathrm{D}_k=\partial\mathrm{D}_{k,1}+...+\partial\mathrm{D}_{k,m(k)}$ (where each $\partial\mathrm{D}_{k,j}$ is a closed contour) (2.8), (2.9) are subject to the boundary conditions of no-normal-flow (kinematical boundary condition)

$$\psi_k(\partial\mathrm{D}_{k,j})=C_{k,j}(t), \tag{2.10}$$

and a viscous (dynamical) boundary condition

$$\frac{\partial^2\psi}{\partial n^2}+\alpha\frac{\partial\psi}{\partial n}=0, \tag{2.11}$$

where $\alpha$ is a constant. This is the mixed boundary condition discussed by Haidvogel et al. [7]. A physically plausible energy balance requires that $\alpha\geq 0$. To our knowledge, there are no physical reasons to prefer some particular value of $\alpha$. The extreme cases of (2.11) known as free-slip ($\alpha=0$) and no-slip ($\alpha=\infty$) will be examined here.

The right-hand sides of (2.10) are constant along closed boundaries. To find unique values of $C_k$ at each point in time, auxiliary conditions insuring consistent budgets of mass, circulation, and energy need to be imposed [19]:

$$\oint_{\partial\mathrm{D}_{k,j}}\left[\frac{\partial}{\partial n}\left(\frac{\partial}{\partial t}+l_k\gamma_k-A_H\nabla^2\right)\psi_k-\mathbf{T}\cdot\hat{\mathbf{s}}\right]\mathrm{d}s=0, \tag{2.12}$$

where $\mathbf{T}=\boldsymbol{\tau}/\rho H_1$, and $\hat{\mathbf{s}}$ is the unit vector tangential to the domain boundary $\partial\mathrm{D}_{kj}$

The rigid-lid assumption automatically conserves total volume. This constraint reduces the number of independent constants in the boundary conditions (2.10) to $N'-1$, where $N'$ is the total number of closed contours in domain's boundaries for all layers. One of the constants is thus chosen to be fixed:

$$C_{1,1} = 0.$$

The remaining constants will be denoted as $C_{k'}(t)$ and the corresponding closed boundaries as $\Gamma_{k'}$, $k' = 1, ...N'-1$.

When all layers occupy simply connected domains $\mathrm{D}_k$ or, in general, domains consisting of simply connected subdomains $\mathrm{D}_{k,i}$, the auxiliary conditions (2.12) can equivalently be written as conservation of mass in each layer:

$$\frac{\mathrm{d}}{\mathrm{d}t}\int\int_{\mathrm{D}_{k,i}}(\psi_k - \psi_{k-1})\mathrm{d}x\mathrm{d}y = 0, \quad k = 2, ..., N \tag{2.13}$$

where $\mathrm{D}_1$ is assumed to be simply connected.

The following notation is used: $\Psi(x,y,t)$ is the vector of streamfunctions $\{\psi_k\}$, $\tilde{\mathbf{q}} = \{\tilde{q}_k\}$ is the vector of PV anomalies, in terms of which (2.9) is written as

$$\nabla^2\psi_k - \frac{f_0^2}{g'_{k-1}H_k}(\psi_k - \psi_{k-1}) - \frac{(1-l_k)f_0^2}{g'_k H_k}(\psi_k - \psi_{k+1}) \;=\; \tilde{q_k} \equiv q_k - \beta y - l_k f_0 \frac{h_b}{H_k} \tag{2.14}$$

Let $\tilde{\Psi} = \{\tilde{\psi}_k\}$ denote the solution of (2.14) subject to homogeneous boundary conditions:

$$(\nabla^2 - A)\tilde{\Psi} = \tilde{\mathbf{q}}, \quad \psi_k(\partial D_k) = 0, \tag{2.15}$$

where $A = \{A_{kk'}(x,y)\}$ is the tridiagonal $N \times N$ matrix of coefficients in (2.14):

$$A = f_0^2 \times \begin{pmatrix} \frac{1-l_1}{g'_1H_1}, & -\frac{1-l_1}{g'_1H_1}, & 0, & \cdots & 0, & 0 \\ -\frac{1}{g'_1H_2}, & \frac{1}{g'_1H_2} + \frac{1-l_2}{g'_2H_2}, & -\frac{1-l_2}{g'_2H_2}, & \cdots & 0, & 0 \\ \vdots & & & & & \vdots \\ 0, & 0, & 0, & \cdots & -\frac{1}{g'_{N-1}H_N}, & \frac{1}{g'_{N-1}H_N} \end{pmatrix} \tag{2.16}$$

The boundary conditions (2.10) are met by adding homogeneous solutions (summation over repeating index is assumed):

$$\Psi = \tilde{\Psi} + \Psi^{(H)}_{k'} C_{k'}, \tag{2.17}$$

where $\{\Psi^{(H)}_{k'}\}$ is the basis of homogeneous solutions:

$$(\nabla^2 - A)\Psi^{(H)}_{k'} = 0, \quad \Psi^{(H)}_{k'}|_{\Gamma_{k''}} = \delta_{k'k''}. \tag{2.18}$$

The latter set of equations needs to be solved only once for given problem parameters.

If we restrict multiply-connected cases to inviscid problems only, the auxiliary conditions (2.12) and (2.13) are of the same form:

$$I_{k'}[\Psi] = I_{k'}[\Psi^{(0)}], \tag{2.19}$$

where $\Psi^{(0)}(x,y) = \Psi(x,y,0)$ is the initial condition, and $I_{k'}[\Psi]$ are the linear functionals (integrals) in the auxiliary conditions ($k' = 1, ..N' - 1$). Substituting (2.17) into (2.19) gives a matrix equation for the unknown constants $C_{k'}$:

$$M_{k'k''}C_{k''} = Y_{k'}, \tag{2.20}$$

where

$$M_{k'k''} = I_{k'}[\Psi^{(H)}_{k''}], \quad Y_{k'} = I_{k'}[\Psi^{(0)}] - I_{k'}[\tilde{\Psi}]$$

Thus the model is completely described by equations (2.8), (2.11), (2.15), (2.17), (2.18) and (2.20).

## 2.3 Numerical solution of the QG equation

Equation (2.8) is discretized in time using a leap-frog scheme:

$$\frac{q_k^{(j+1)} - q_k^{(j-1)}}{2\Delta t} = -\mathrm{J}(\psi_k^{(j)}, q_k^{(j)}) + F + D[\psi_k^{(j-1)}]; \tag{2.21}$$

Here $F = \delta_{k,1} f_0 w_e / H_1$, $D[\psi_k]$ is the sum of dissipative terms in the right-hand side of (2.8), and the superscript denotes the time in time steps $\Delta t$.

Discretization in space is done with finite differences on a regular Cartesian grid

$$\{x_n, y_j\} = \{n\Delta x, j\Delta y\}, \tag{2.22}$$

where $\Delta y = \Delta x$. If irregular boundaries are present they are discretized by zonal or meridional segments. New values of PV, $q_k^{(j+1)}$, are calculated at interior nodes, using a second order Arakawa scheme ([1]) for the advective term $\mathrm{J}(\psi_k, q_k)$.

The presence of finite topography does not complicate the procedure of calculating $q_k^{(j+1)}$ which is done in each layer, k, independently. The only subtlety associated with the finite topography is involved in solving the linear problem (2.15) of inverting $q_k^{(j+1)}$ (known at the

interior grid nodes) into streamfunctions $\psi_k^{(j+1)}$. The Laplacian in (2.15) is discretized by central differences:

$$\nabla^2\psi \;=\; \nabla_2^2\psi \;+\; O(\Delta x^2), \tag{2.23}$$

where

$$\nabla_2^2\psi(x_n, y_j) = \frac{\psi(x_{n+1}, y_j) + \psi(x_{n-1}, y_j) + \psi(x_n, y_{j+1}) + \psi(x_n, y_{j-1}) - 4\psi(x_n, y_j)}{\Delta x^2}$$

The same scheme is used to discretize the frictional term $D[\psi_k^{(j-1)}]$. The latter requires boundary values of $\nabla^2\psi_k^{(j-1)}$ (to calculate $\nabla^4\psi_k^{(j-1)}$ in the interior) which are calculated with dynamic boundary conditions (2.11) taken into account:

$$\nabla^2\psi(\mathbf{x_b}) = \nabla_{1b}^2\psi(\mathbf{x_b}) + O(\Delta x),$$

where

$$\nabla_{1b}^2\psi(\mathbf{x_b}) = \begin{cases} 0, & \text{free-slip or corner points,} \\ 2\frac{\psi(\mathbf{x_n})-\psi(\mathbf{x_b})}{\Delta x^2} & \text{otherwise,} \end{cases}$$

$\mathbf{x_b}$ is the boundary node and $\mathbf{x_n}$ is the neighboring interior node. The latter formula is also used to calculate $q_k^{(j+1)}$ at the boundary after solving (2.15). (The no-slip case is verified by substituting $\psi \sim x^p$ or $\psi \sim y^p$ for $p = 0$ and $p = 2$)

Terms containing discontinuous coefficients in (2.8), (2.15) and (2.18) must be treated specially. In short, they are discretized in the finite-volume sense: the value of the coefficient at a given grid node is obtained by area-averaging the discontinuous coefficient over the neighboring grid cells. This method is implemented in this thesis for the simple case of one-dimensional topography. Appendix A describes a procedure of solving the discretized equations (2.15), (2.18) in the presence of general topography.

## 2.4 Simple geometry case

Two cases of one-dimensional topography will be considered: (a) a straight periodic channel with a topographic shelf parallel to the channel walls (see Fig. 3.7), and (b) a rectangular basin with a shelf in the western part of the domain (see Fig. 4.1).

### 2.4.1 Periodic channel

Let $N_x \times N_y$ be the size of the grid where $l = 0, ..., N_x - 1$ numbers the grid nodes in the along-channel ($x$) direction, and $j = 1, ..., N_y$, in the across-channel direction ($y$) direction.

Let $j = b$ correspond to the topographic break, where the number of active layers jumps from $N$ for $y < y_b$ to $n < N$ for $y > y_b$, and $A_{n,n+1}$ in (2.15) jumps from $-\frac{f_0^2}{g'_n H_n}$ to 0. Then the finite-volume discretized form of (2.15) is written

$$\nabla_2^2 \tilde{\Psi} - \overline{A}\tilde{\Psi} = \tilde{\mathbf{q}}, \tag{2.24}$$

where $\overline{A}$ is obtained from $A$ by averaging over the neighboring grid nodes:

$$\overline{A}_{n,n+1}(x_l, y_j) = \begin{cases} -\frac{f_0^2}{g'_n H_n}, & j < b, \\ -\frac{f_0^2}{2g'_n H_n}, & j = b, \\ 0, & j > b \end{cases}$$

(other elements of $A$ are not affected by the discretization)

The streamfunction and PV anomaly fields are decomposed into discrete Fourier modes:

$$\tilde{\mathbf{q}}(x_l, y_j) = \sum_{m=-N_x/2}^{N_x/2-1} \tilde{\mathbf{q}}^{(m)}(y_j) \exp\left(i\frac{2\pi m l}{N_x}\right),$$

$$\tilde{\Psi}(x_l, y_j) = \sum_{m=-N_x/2}^{N_x/2-1} \tilde{\Psi}^{(m)}(y_j) \exp\left(i\frac{2\pi m l}{N_x}\right),$$

and since $\overline{A}$ does not change in the $x$ direction, (2.24) is written in Fourier space as (dropping $\tilde{}$)

$$\widehat{\nabla_2^2}\Psi^{(m)} - \overline{A}\Psi^{(m)} = \mathbf{q}^{(m)}, \tag{2.25}$$

where

$$\widehat{\nabla_2^2}\psi_k^{(m)}(y_j) = \frac{1}{(\Delta x)^2}\left[\left(-4 + 2\cos\frac{2\pi m}{N_x}\right)\psi_k^{(m)}(y_j) + \psi_k^{(m)}(y_{j-1}) + \psi_k^{(m)}(y_{j+1})\right]$$

The PV anomaly is transformed into Fourier space ($N_x$ is chosen to be a power of 2). Then (2.25), linear equations with non-constant coefficients, are solved for each $m$ by a direct solver. (A pentadiagonal solver could be used. We used a one-dimensional analog of the general procedure described in Appendix A that reduced the problem to several smaller tridiagonal matrix problems). Since the homogeneous solutions are one-dimensional in this case (and can be found analytically), only the $m = 0$ mode is corrected to satisfy the boundary conditions (2.10). The corrected solution of (2.25) is then transformed back to physical space.

### 2.4.2 Basin with a shelf

The discretized equation (2.15) can be solved by a scheme similar to the FACR algorithm [9],[33], where decomposition into sine modes is employed. We have

$$\tilde{\mathbf{q}}(x_i, y_j) = \sum_{m=0}^{N_y} \tilde{\mathbf{q}}^{(m)}(x_i) \sin\left(\frac{\pi m j}{N_y}\right),$$

$$\tilde{\Psi}(x_i, y_j) = \sum_{m=0}^{N_y} \tilde{\Psi}^{(m)}(x_i) \sin\left(\frac{\pi m j}{N_y}\right),$$

where $j = 0, ..N_y$ numbers the grid nodes in the meridional direction. Substituting the expressions above into the discretized form of (2.15) yields (dropping $\tilde{}$)

$$\widehat{\nabla_2^2}\Psi^{(m)} - \overline{A}\Psi^{(m)} = \mathbf{q}^{(m)}, \tag{2.26}$$

where in this case

$$\widehat{\nabla_2^2}\psi_k^{(m)}(x_i) = \frac{1}{(\Delta x)^2}\left[\left(-4 + 2\cos\frac{\pi m}{N_y}\right)\psi_k^{(m)}(x_i) + \psi_k^{(m)}(x_{i-1}) + \psi_k^{(m)}(x_{i+1})\right]$$

Equations (2.26) are solved by a solver similar to the one used for solving (2.25). Homogeneous solutions are now 2-dimensional but symmetric - they consist of sine modes for which $m$ is odd. To find the homogeneous solutions a change of variables is used

$$\psi_1 = \phi_1, \quad \psi_k = C_k + \phi_k, \ k = 2, ...N,$$

which reduces the problem to (2.15).

# CHAPTER 3

# WAVES OVER ABRUPT TOPOGRAPHY

## 3.1 Introduction

Lateral disturbances over abrupt and confined topography can be found over the Mid-Atlantic Bight continental slope. Pickart [24] argued that they were generated by the Gulf Stream variations and propagated along the slope pseudo-westward (to the left facing the continental shelf)

Dewar and Leonov [6] analytically examined wave evolution of such disturbances. First, *weak topography* case was considered (fractional fluid depth change is small across the slope), where standard QG applies, and the analysis technique was introduced. The technique was then translated to finite topography case, where the fluid on an infinite f-plane was assumed to consist of two active layers of depths $H_1$ and $H_2$ 'south' of the shelf break ($y < 0$), and of one active layer of depth $H_1 - h_0$ 'north' of the shelf break ($y > 0$). In short, this study examined analytically the same setting as the numerical model designed in Chapter 2. Here, the numerical model is applied to the waves problem described in [6] in order to verify the model against known solutions, and to extend the waves study into the strongly nonlinear regime.

## 3.2 Weakly-nonlinear analysis

### 3.2.1 Wave evolution in the finite topography case.

The initial value problem solved here is illustrated in Fig. 3.1. The lower layer potential vorticity is always zero. At rest the upper layer PV is piecewise constant with a front $L(x,t)$ at the shelf break. PV conservation implies that the front, when perturbed by an initial disturbance (for example, an incident Rossby wave), will move with the fluid:

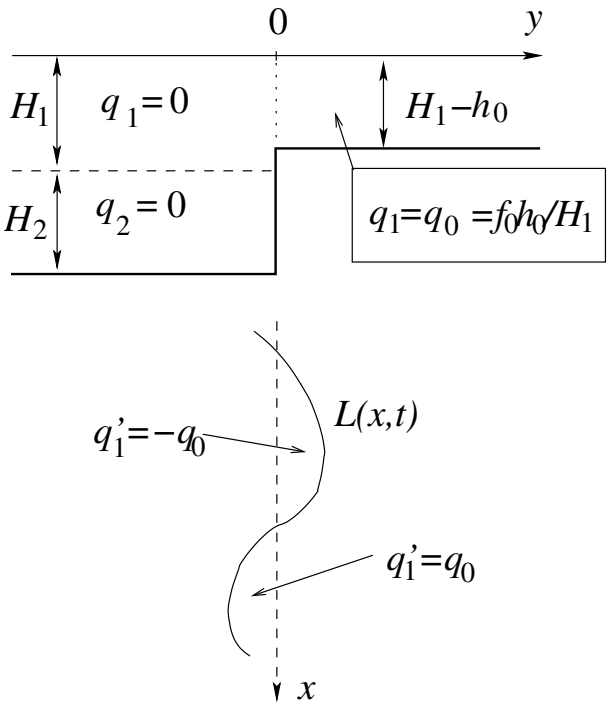


**Figure 3.1**. Trapped topographic wave over finite topography: system at rest (above); perturbed upper layer PV front (below). The two values of upper layer PV: 0, $q_0$ are separated by the front $L(x,t)$. Regions between unperturbed ($y = 0$) and perturbed ($y = L(x,t)$) front positions have non-zero PV anomaly $q_1' = \pm q_0$

$$L_t + uL_x = v,$$

where $(u, v)$ is the horizontal velocity at the front. Using the upper layer geostrophic streamfunction $\psi_1$, the latter equation can be written as

$$\partial_t L = \partial_x \psi_1(x, L, t) \tag{3.1}$$

To solve the frontal equation (3.1), one needs to invert the upper layer PV anomaly given by

$$q_1' = \begin{cases} -q_0 \mathrm{sign} y, & 0 < yL < L^2, \\ 0, & \text{otherwise} \end{cases} \tag{3.2}$$

where $q_0 = f_0 h_0 / H_1$, into streamfunctions. The linear elliptic equations for streamfunctions can be written separately for offshelf and onshelf parts of the plane. For $y < 0$ the problem

is decoupled into barotropic and baroclinic modes ($\psi_b = (H_1\psi_1 + H_2\psi_2)/H$, $\psi_c = \psi_1 - \psi_2$, where $H = H_1 + H_2$):

$$\begin{array}{lcl} H\nabla^2\psi_b & = & H_1 q_1', \\ (\nabla^2 - R^{-2})\psi_c & = & q_1', \end{array} \tag{3.3}$$

where $R$ is the baroclinic deformation radius: $R^{-2} = \frac{f_0^2}{g'}\left(\frac{1}{H_1} + \frac{1}{H_2}\right)$, and $\nabla = \{\partial_x, \partial_y\}$. A rigid upper lid is employed. For $y > 0$, we have

$$\nabla^2\psi_{1(+)} = q_1', \tag{3.4}$$

At the shelf break ($y = 0$) the following boundary conditions apply: no-normal flow in the lower layer, and matching the partially-valid solutions in the upper layer (the upper layer PV is finite everywhere which implies continuity of the stream function with its first derivatives):

$$\begin{array}{lcl} \psi_{2(-)} & = & 0, \\ \psi_{1(-)} & = & \psi_{1(+)}, \\ \partial_y\psi_{1(-)} & = & \partial_y\psi_{1(+)}, \end{array}$$

where we substitute $\psi_1 = \psi_b + \frac{H_2}{H}\psi_c$, $\psi_2 = \psi_b - \frac{H_1}{H}\psi_c$:

$$\begin{array}{lcl} H\psi_b - H_1\psi_c & = & 0, \\ H\psi_b + H_2\psi_c & = & H\psi_{1(+)}, \\ \partial_y(H\psi_b + H_2\psi_c) & = & H\partial_y\psi_{1(+)}. \end{array} \tag{3.5}$$

Using Green functions $G_b$ and $G_c$ of the operators $\nabla^2$ and $\nabla^2 - R^{-2}$ on the infinite plane, defined by

$$\nabla^2 G_b(x,y) = \delta(x)\delta(y), \tag{3.6}$$

$$(\nabla^2 - R^{-2})G_c(x,y) = \delta(x)\delta(y), \tag{3.7}$$

a formal solution to (3.3)-(3.5) can be written:

$$\begin{array}{lll} \psi_b = & \frac{H_1}{H} q_0 \int_{-\infty}^{\infty}\int_{L_-}^{0} G_b(x-\xi, y-\eta)\,\mathrm{d}\eta\,\mathrm{d}\xi & + \int_{-\infty}^{\infty} \theta_b(\xi) G_b(x-\xi, y)\,\mathrm{d}\xi, \\ \psi_c = & q_0 \int_{-\infty}^{\infty}\int_{L_-}^{0} G_c(x-\xi, y-\eta)\,\mathrm{d}\eta\,\mathrm{d}\xi & + \int_{-\infty}^{\infty} \theta_c(\xi) G_c(x-\xi, y)\,\mathrm{d}\xi, \\ \psi_{1(+)} = & -q_0 \int_{-\infty}^{\infty}\int_{0}^{L_+} G_b(x-\xi, y-\eta)\,\mathrm{d}\eta\,\mathrm{d}\xi & + \int_{-\infty}^{\infty} \theta_1(\xi) G_b(x-\xi, y)\,\mathrm{d}\xi \end{array} \tag{3.8}$$

Here $L_+ = (L + |L|)/2$, $L_- = (L - |L|)/2$ are onshelf and offshelf lobes of the frontal curve (see Fig. 3.2). The first terms (area integrals) thus satisfy (3.3) and (3.4). Second terms

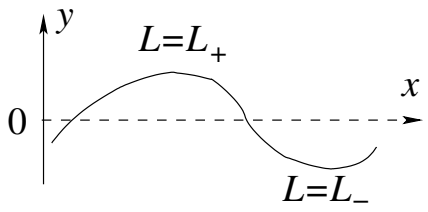


**Figure 3.2**. On-shelf ($L_+ \geq 0$) and offshelf ($L_- \leq 0$) lobes of the frontal curve $L = L_+ + L_-$

(line integrals), which do not change the right-hand sides of (3.3) and (3.4), are contributions of artificial sources of PV located at the shelf break. Their amplitudes $\theta_b$, $\theta_c$, $\theta_1$ are adjusted to satisfy the boundary conditions (3.5).

A formal solution similar to (3.8) was used by Thompson [34] in a modified contour dynamics method. The front there did not have to be represented by a single-valued function of $x$. Dewar and Leonov [6] focused on small-steepness disturbances (necessarily single-valued functions of $x$) and examined an approximate form of the frontal equation (3.1). The streamfunction in the right-hand side of (3.1) can be Taylor expanded as

$$\psi_1(x, L, t) \;=\; \psi_1(x, 0, t) + \psi_{1y}(x, 0, t)L + \frac{1}{2}\psi_{1yy}(x, 0\pm, t)L^2 + O(L^3) \tag{3.9}$$

Dewar and Leonov [6] retained terms linear and quadratic in wave steepness in the first two quantities in the right-hand side of (3.9), and examined the properties of the resulting equation as a weakly-nonlinear model of waves on topography. The third term, however, not discussed in [6], can also contribute to the streamfunction at second order in wave steepness. To see this, suppose $L(x, t_0) = L_0 \cos(kx)$, where $kL_0 \ll 1$. Then $\psi_{1yy} \approx \nabla^2\psi_1 = q_1'$, and the third term is formally quadratic. A more accurate representation of the wave equation thus requires all three right-hand side contributions shown in (3.9). The third term is thus retained here.

The formal solution (3.8) is simplified by using Fourier transforms. In Fourier space, the boundary integrals become products so the weights $\theta$ can be found exactly, and the terms in (3.9) can be written in closed form. Details are given in Appendix B. As a result, a weakly-nonlinear equation for $L$ is derived:

$$\partial_t \widehat{L} \;=\; ik\,\frac{q_0}{2}\left(\frac{2H\mathrm{sign}k\widehat{L} \;-\; Hk\widehat{L|L|} \;+\; [2Hk+2H_2(\kappa-k)]\,\widehat{L_-^2}}{(2H-H_2)k+H_2\kappa} + \frac{\widehat{\theta_{1(\mathrm{lin})}L}}{q_0}\right), \qquad (3.10)$$

where

$$\widehat{f}(k) = \int_{-\infty}^{\infty} f(x)e^{-ikx}\mathrm{d}x, \qquad \kappa = \mathrm{sign}k\sqrt{k^2+R^{-2}},$$

and $\theta_{1(\mathrm{lin})}$ is defined in (B.17).

In the short-wave limit $k^2 \gg R^{-2}$, second layer becomes unimportant, the dominant terms in (3.10) describe waves in the barotropic case ($H_2 = 0$):

$$\partial_t \widehat{L} \;=\; i\mathrm{sign}k\frac{q_0}{2}\widehat{L} - ik\frac{q_0}{4}\widehat{L|L|}, \qquad (3.11)$$

or in physical space:

$$L_t + \frac{q_0}{2}\int_{-\infty}^{\infty}\frac{L(x-\xi)}{x-\xi}\mathrm{d}\xi + \frac{q_0}{4}(L|L|)_x = 0 \qquad (3.12)$$

Other limits generally do not yield closed form solutions.

### 3.2.2 Dispersion relation, comparison with the weak topography case

Linearizing the wave equation (3.10) for small amplitude waves of the form $\sim e^{i(kx-\omega t)}$ yields the dispersion relation:

$$\omega = -q_0\frac{Hk}{(2H-H_2)|k| + H_2\sqrt{k^2+R^{-2}}} \qquad (3.13)$$

Both phase and energy propagate pseudo-westward (to the left facing the shelf), phase and group speeds converge to $q_0\frac{H}{H_2}R$ in the long-wave limit.

It is interesting to compare this result to the baroclinic dispersion relation obtained in [6] for the weak topography case, where the topography consisted of a narrow slope crudely represented by two steps (Fig. 3.4), under a two-layer fluid. The dispersion relation for the sinuous mode is a sum of a barotropic and a baroclinic term. The result is shown in Fig. 3.5. In the abrupt step limit ($a = 0$) the dispersion relation is given by

$$\omega = -\frac{q_0}{2}\left(\frac{H_2}{H}\mathrm{sign}k + \frac{H_1}{H}\frac{k}{\sqrt{k^2+R^{-2}}}\right) \qquad (3.14)$$

where $q_0 = f_0h_0/H_2$. In this case the barotropic term corresponds to the Rhines' double Kelvin wave [29]. The baroclinic term is familiar from the dispersion relation for reduced-gravity waves on a jet, obtained by Pratt and Stern [25]. The resulting wave has a

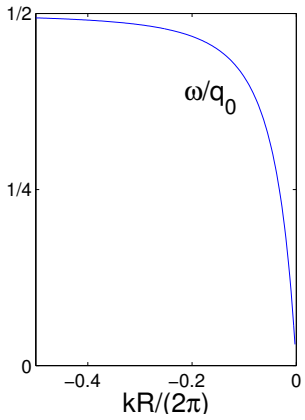


**Figure 3.3**. Finite-topography dispersion relation (3.13) for $H_1 = H_2$

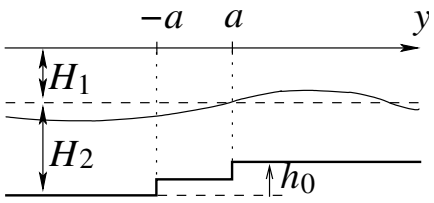


**Figure 3.4**. Weak topography problem

pseudo-westward group speed due to the baroclinic term. The barotropic term is constant because of the rigid lid approximation which results in infinite phase speed in the long-wave limit. Note that this property is lost for the case of finite amplitude topography.

Thus finite topography "filters out" barotropic dynamics for long waves: they are non-dispersive with speed defined by the baroclinic deformation radius.

### 3.2.3 Wave steepening

Although in the short-wave limit, nonlinear effects are local and symmetric:

$$(\partial_t L)_{(\text{quad})} = -\frac{q_0}{4}\partial_x(L|L|),$$

which results in backward (pseudo-eastward) steepening, the quadratic terms in (3.10) describe steepening which is generally non-local (steepening at a given point depends on

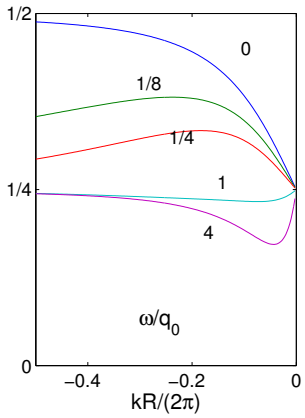


**Figure 3.5**. Weak-topography dispersion relation for $H_1 = H_2$; $a/R = 0,\ 1/8,\ 1/4,\ 1,\ 4$

non-local properties of the front), and asymmetric with respect to the onshelf − offshelf direction (i.e. the steepening on the offshore side is different from the steepening on the onshore side).

The propagation of localized disturbances is analyzed here by integrating the weakly-nonlinear equation (3.10) on a 8192-point periodic grid of the length 7000 km. The constant parameters are: $H_1 = H_2 = 1000$ m, $h_0/H_1 = 0.025$, $R = 20$ km, $f_0 = 8.3 \times 10^{-5} s^{-1}$. These parameters are roughly representative of a mid-latitude continental shelf. The initial front position was set to $L(x, 0) = L_0 \exp(-x^2/x_e^2)$. The evolution of two initial disturbances that differ in sign of $L_0$

The wave in both cases propagates pseudo-westward. The long-wave limit group speed $\frac{h_0 H}{H_1 H_2} f_0 R \approx 7$ km/day is offset both by dispersion (the group speed is smaller at finite wavelengths) and by backward steepening. The latter is more pronounced in the case of an offshelf initial disturbance (Fig 3.6b), which results in a smaller effective propagation speed.

## 3.3 Channel calculations

In this section the problem of trapped topographic waves over finite topography is addressed numerically using the modified QG model applied to a periodic channel with a shelf.

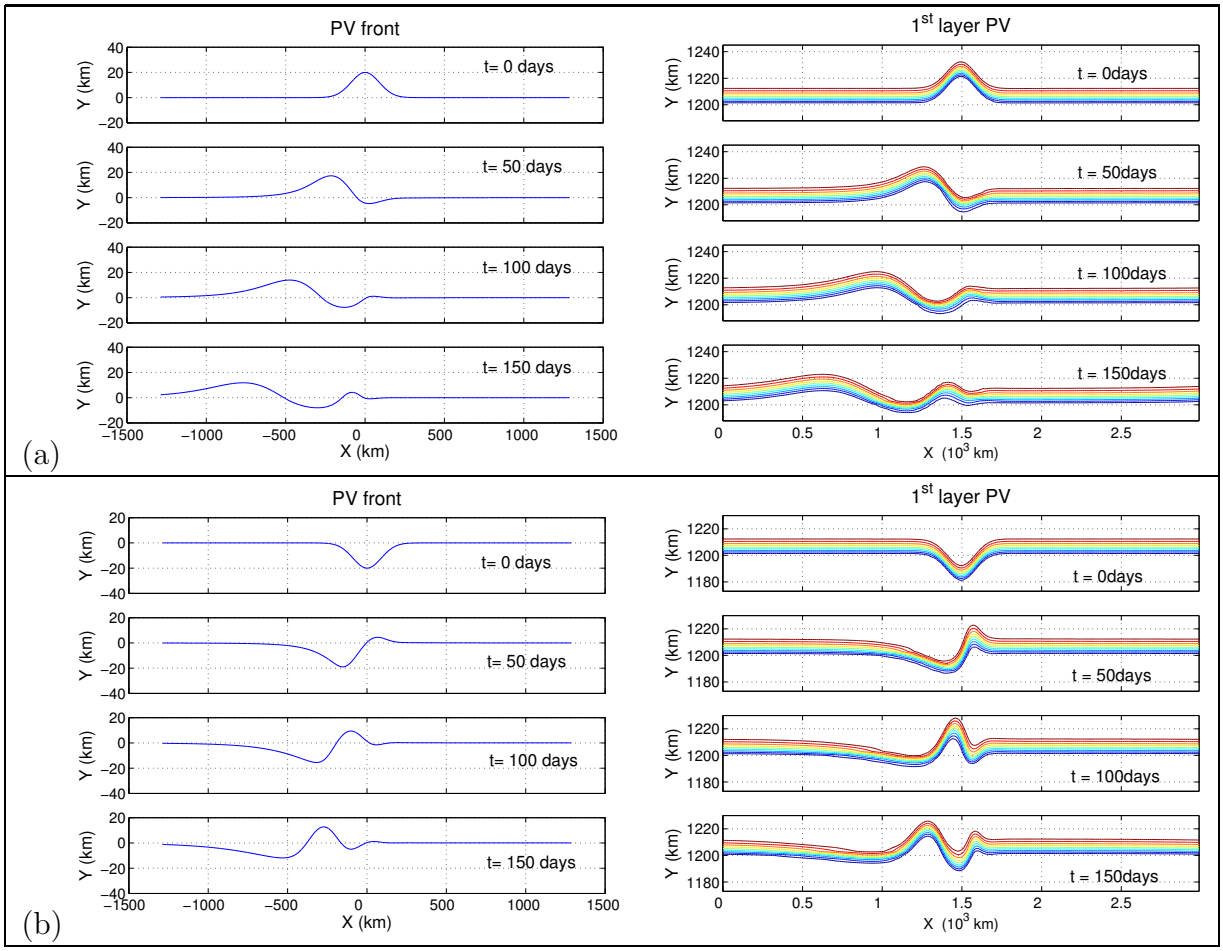


**Figure 3.6**. Front evolution from weakly-nonlinear theory (left) and channel calculation results from Experiment 1 (right) for same sets of parameters: $x_e$ =125 km; (a) $L_0$ =20 km, (b) $L_0$ =-20 km

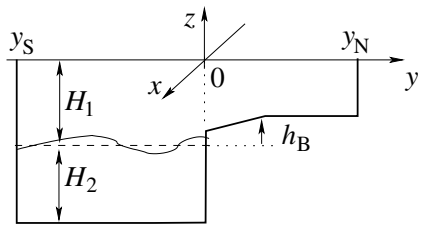


**Figure 3.7**. Model geometry in the channel calculations

**Table 3.1**. Channel model parameters

| **parameter** | **experiment 1** | **experiment 2** |
|---|---|---|
| grid size (nodes, $N_x \times N_y$) | $1024 \times 801$ | |
| grid resolution | 3 km | |
| reduced gravity | 0.0055 $\mathrm{m}^2/\mathrm{s}$ | |
| Coriolis parameter $f_0$ | $8.3\times10^{-5}$ $\mathrm{s}^{-1}$ | |
| topographic lateral scale $y_B$ | 150 km | |
| topographic height $h_B/H_1$ | 0.0025 | |
| layer depths $H_1$, $H_2$ | 1000 m, 1000m | 500 m, 1500 m |

### 3.3.1 The model

Inviscid QG equations on the f-plane are written for the model geometry shown in Fig. 3.7.

$$\begin{array}{ll} (\partial_t + J(\psi_1, \cdot))\, q_1 & = 0, \quad y_S < y < y_N, \\ (\partial_t + J(\psi_2, \cdot))\, q_2 & = 0, \quad y_S < y < 0, \end{array} \tag{3.15}$$

where

$$\begin{array}{ll} q_1 = & \nabla^2\psi_1 - (1 - s(y))\lambda_1(\psi_1 - \psi_2) + \frac{f_0}{H_1} s(y) h_B(y), \\ q_2 = & \nabla^2\psi_2 + \lambda_2(\psi_1 - \psi_2) + \frac{f_0}{H_2} h_B(y), \quad \lambda_k = \frac{f_0^2}{g' H_k}, \end{array} \tag{3.16}$$

where $s(y)$ is the Heaviside step function.

The discretization and numerical procedure are described in Chapter 2. The model has been implemented for a periodic channel with a shelf break equidistant from the walls. With the shelf located at $y = 0$, the topography profile is given by

$$h_B(y) = h_0 s(y) \tanh(y/y_B). \tag{3.17}$$

Several experiments have been performed with different initial conditions defined by PV:

$$q_1(x, y, 0) = \frac{f_0}{H_1} h_B(y - L_0 e^{-x^2/x_e^2}), \quad q_2(x, y, 0) = 0,$$

The initial streamfunction is found by numerically inverting the initial PV. The model parameters are given in Table 3.1

### 3.3.2 Experiment 1 (small steepness): testing against analytical results

The numerical model described above is applied here to the initial disturbances for which frontal solutions were obtained. Figure 3.6 shows side-by-side snapshot comparison of the frontal solutions and gridpoint numerical solutions for the same initial disturbances. Propagation speeds of the main wave crests are within 20% for both initial disturbances. The magnitudes of the slowest-propagating secondary wave crests agree reasonably well both in Fig. 3.6a (onshelf initial disturbance) and in Fig. 3.6b (offshefl initial disturbance). The differences may be attributed to the differences in topography: the frontal problem formulation does not include a slope present in the numerical model, and are small compared to the asymmetry between the examples themselves.

The basic conclusions drawn from this comparison are that the weakly-nonlinear equation accurately describes the evolution of small-steepness disturbances (both linear and quadratic terms in the equation are involved since there is substantial asymmetry between the examples) and, on the other hand, that the finite-topography QG numerical model is accurate: the numerical procedure is verified against an analytical result.

### 3.3.3 Experiment 2: wave overturning

Here steeper disturbances outside the limits of the weakly-nonlinear theory are analyzed numerically using the model described earlier, with parameters given in Table 3.1. Fig. (3.8) shows evolution of two initial disturbances of different signs. The onshelf−offshelf asymmetry evident in the weak steepness regime is even more pronounced for the strong disturbances. Both onshelf and offshelf disturbance develop into a backward-steepening wave that eventually overturns. The onshelf disturbance results in filamentation of the onshelf fluid into the offshelf regime. The offshelf initial disturbance takes a little longer to overturn, and results in separation of the offshelf fluid onto the shelf in the form of eddy detachment. This process is qualitatively similar to the eddy detachment observed in the contour dynamics calculations by Pratt and Stern [25], where the PV front was associated with the discontinuity in the shear rather than abrupt topography. Some possible implications of these results and directions of future work are discussed in Chapter 5.

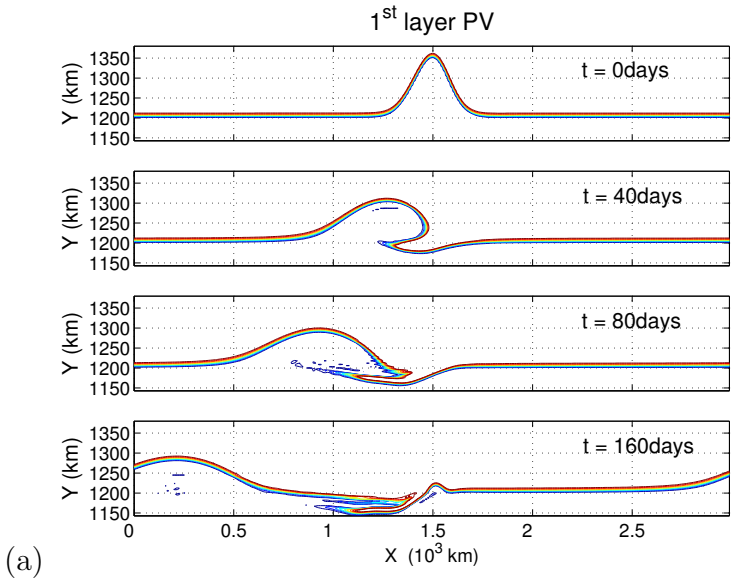


(a)

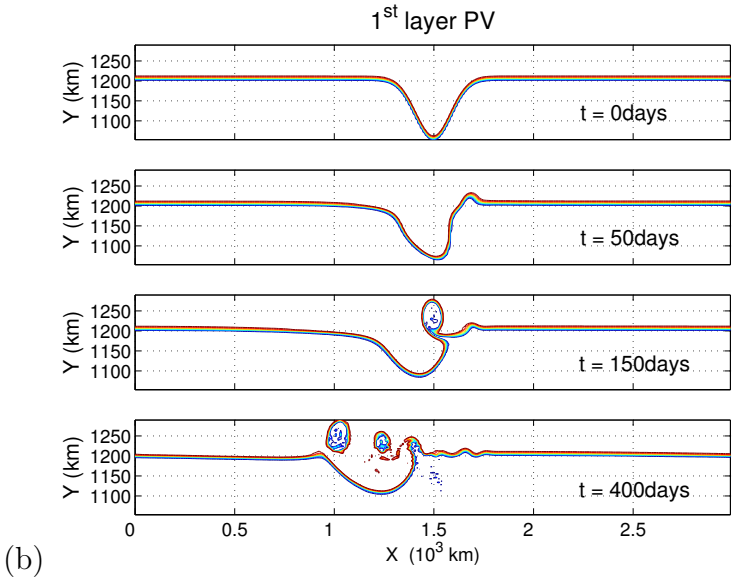


(b)

**Figure 3.8**. Evolution of initial disturbance: $x_e$ =125 km; (a) $L_0$ =150 km, (b) $L_0$ =-150 km

# CHAPTER 4

# WIND-DRIVEN CIRCULATION: COMPARISON WITH STANDARD QG

In this chapter variability of the wind-driven ocean circulation is analyzed in the presence of finite topography using the modified QG approach formulated in Chapter 2 and tested in Chapter 3. We build upon the study by Berloff and McWilliams [2] where a standard QG model was used to examine the onset of variability as the Reynolds number (Re) increases. It is known [7] that time-mean circulation and eddy fields in the QG model change significantly as the mixed boundary condition coefficient $\alpha$ changes from 0 (free-slip limit) to $\infty$ (no-slip limit). As $\alpha$ increases, the role of lateral friction as the main kinetic energy dissipater is increased [7]. The study by Berloff and McWilliams [2] included consideration of a reduced gravity model where lateral friction is the only dissipative mechanism. They also considered a 2-layer QG model. In a classical multilayer QG model, the bottom drag is confined to the lower layer, and the model still relies on lateral friction. If $\alpha$ in (2.11) is small (close to the free-slip limit), the model produces so-called "inertial runaway" solutions at high Re, characterized by the gyres totally occupied by inertial recirculations [27]. This is a practical reason for the choice of a boundary condition regime close to no-slip in studies using QG. No-slip boundary condition was chosen in [2].

The modification of QG to include finite topography is consistent with the fact that the observed oceans have bottom topography everywhere and no vertical walls. In the finite-topography QG model the role of bottom drag is increased since it is no longer restricted to the lower layer. This implies the hypothesis tested here that the finite-topography model is not as sensitive to $\alpha$ as the standard QG. Time-mean circulation, mean-field effects of eddies, and low-frequency variability are analyzed here. The results are also compared to the classical QG model results for different values of $\alpha$ to find values better parametrizing finite topography.

## 4.1 Description of experiments

This chapter compares and analyzes results of basin-scale simulations of the wind-driven circulation done with two models:

1. Shelf model: a 3-layer QG model with a topographic shelf in the upper layer. The basin geometry (Fig. 4.1) is rectangular with the shelf parallel to the meridional boundaries. The lower layer bottom is flat; the shelf has topographic variations above the undisturbed interface (shown as an abrupt step in Fig. 4.1), given as

$$h_B(x) = h_0 \tanh \frac{L_S - x}{a}, \quad x < L_S, \tag{4.1}$$

   where $L_S$ is the shelf width, $a$ is the width of the slope, $h_0$ is the height of the flat part of the shelf above the mean layer interface.

2. No-shelf model: a standard QG model for the same basin with the shelf part of the upper layer removed.

The two sets of experiments will be referred to as "Shelf experiments" and "No-shelf experiments". The parameters defining basin geometry and stratification are given in Table 4.1. Discretized equations (2.8), (2.9) are solved using the numerical procedure described in Chapter 2. The Ekman forcing is given by

$$w_e = -w_0 \sin \frac{2\pi y}{L_y}, \quad 0 < y < L_y \tag{4.2}$$

Constant parameters of the model are chosen to qualitatively represent the North Atlantic with its subtropical and subpolar gyres, and are comparable to the parameters chosen by Berloff and McWilliams [2]. Lateral friction and $\alpha$ are varied between six different parameter regimes (labeled a - f) in each of the two models. Tables 4.2-3 list the constant and regime-specific model parameters. A rigid upper lid approximation is employed, so the deformation radii calculated from reduced gravities and layer thicknesses (as inverse square roots of eigenvalues of the vortex tube stretching coefficients matrix A defined in (2.16)) are $R_0 = \infty$, $R_1 = 36$ km, $R_2 = 19$ km. These values are comparable to those of the Atlantic and Pacific mid-latitudes, although the real ocean exhibits horizontal variations.

**Table 4.1**. Basin parameters

| **parameter** | | value |
|---|---|---|
| deep interior size | $L_x,\ L_y$ | 2790km, 3190 km |
| shelf width | $L_s$ | 400 km |
| layer thicknesses | $H_1,\ H_2,\ H_3$ | 400 m, 500 m, 900 m |
| reduced gravities | $g_1', g_2'$ | 0.021 m/s$^2$, 0.0105 m/s$^2$ |
| shelf top. amplitude | $h_0$ | 100 m |
| shelf top. scale | $a$ | 100 km |

The Reynolds number based on the interior velocity (defined as Re=$\frac{f_0 w_0 L_x}{\beta A_H H_1}$) occupies the range from 200 to 1400, which is much higher than what Berloff and McWilliams [2] had, due to both smaller lateral viscosities and much stronger Ekman forcing. Our parameters correspond to the Munk scale $\delta_M = (A_H/\beta)^{1/3}$ ranging from 18 to 35 km and inertial scale $\delta_I = \frac{1}{\beta}\left(\frac{f_0 w_e}{H_1}\right)^{1/2}$=55 km. The consideration of relatively high Reynolds number regimes is consistent with testing the hypothesis of reduced sensitivity to $\alpha$ in the finite-topography model.

In each of the 12 cases the model was run for at least 80 years after an initial 20 yr. spin-up. Model output consisted of daily levels of total kinetic and potential energies, layer streamfunction, PV, kinetic energy, $\frac{(\nabla\psi_k)^2}{2}$, and PV flux convergence, $-J(\psi_k, q_k)$, calculated as 50 day means of daily snapshots in reduced resolution (averaged over 25 km $\times$ 25 km boxes), time-mean streamfunctions and PV's in full resolution (513$\times$513 for the Shelf experiments, 419$\times$513 for the No-shelf experiments), computed using data after the spin-up.

An analysis of results of the two models is given in subsequent sections. By examining time-mean behavior and variability in different parameter regimes, sensitivity to the partial-slip parameter $\alpha$ is checked: free-slip regimes (a, b, c) are compared to no-slip regimes (d, e, f) in each of the two experiments. We also quantify the role of the continental shelf in setting the dynamics of the wind-driven circulation.

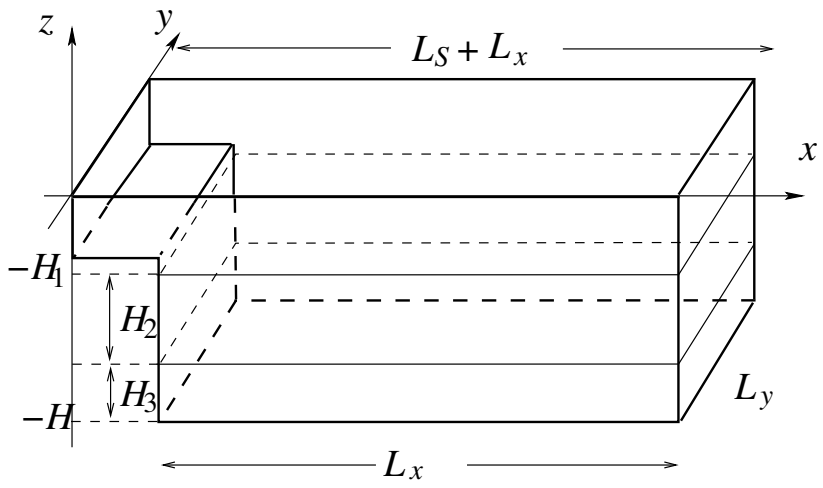


**Figure 4.1**. Basin geometry for the shelf model

## 4.2 Time-mean circulation: descriptive comparison

Fig. 4.2 and 4.3 show time-mean barotropic streamfunctions ($\psi_b = \sum_k H_k \psi_k$) in the Shelf and No-shelf experiments. The Shelf results exhibit far less sensitivity to the imposition of free-slip or no-slip boundary conditions than do the No-shelf results. This applies both to net transports and shapes of the stream lines, even at low Reynolds number (Re): regimes a, d. The agreement becomes better at higher Re (regimes b vs. e and c vs. f), except for the wall-trapped recirculation gyres near the zonal boundaries present in the free-slip regimes b,c and absent in the no-slip regimes e,f. These recirculations may be removed if the domain is extended in the meridional direction while confining non-zero wind forcing to the original domain. The No-shelf experiments produces well-known results that are very sensitive to the partial-slip parameter $\alpha$ [7]: both net transports and circulation patterns are substantially different over the whole range of Re. Upper layer stream functions are plotted in Fig. 4.4 and 4.5. Their comparison also shows reduced sensitivity to $\alpha$ in the Shelf experiments, especially at higher Re. All regimes in the Shelf experiments produce comparable levels of net time-mean barotropic transport around 140 Sv (Fig. 4.6). (For comparison, the observed North Atlantic Gulf Stream transport reaches $\approx$ 150 Sv at $60°W$ [11].) These are close to the no-slip levels in the No-shelf experiments. The linear Sverdrupian transport based on

**Table 4.2**. Constant model parameters

| **parameter** | | **value**(Shelf experiments) | **value**(No-shelf experiments) |
|---|---|---|---|
| Coriolis parameter | $f_0$ | $8.3 \times 10^{-5}$ s $^{-1}$ | |
| | $\beta$ | $1.66 \times 10^{-11}$ (ms) $^{-1}$ | |
| wind forcing amplitude | $w_0$ | $4.0{\times}10^{-6}$ m/s | |
| bottom drag (upper layer) | $r_s$ | $10^{-7}$ s$^{-1}$ | |
| bottom drag (lower layer) | $r_b$ | $10^{-8}$ s$^{-1}$ | $10^{-7}$ s$^{-1}$ |
| horizontal resolution | $\Delta x$ | 6.23 km | |
| time step | $\Delta t$ | 20 min | |

**Table 4.3**. Parameter regimes defined by lateral friction $A_H$ and type of dynamic boundary condition: free-slip ($\alpha = 0$) or no-slip ($\alpha = \infty$)

| **parameter regime** | $A_H$ (m$^2$/s), $Re = \frac{f_0 L_x w_e}{\beta H_1 A_H}$ | $\alpha$ |
|---|---|---|
| a | 700, 200 | 0 |
| b | 400, 350 | 0 |
| c | 100, 1400 | 0 |
| d | 700, 200 | $\infty$ |
| e | 400, 350 | $\infty$ |
| f | 100, 1400 | $\infty$ |

the model parameters is $T = f_0 w_0 L_x/\beta = 56Sv$. This unusually large number is due to the strong bottom drag and strong Ekman forcing, but was necessary to achieve Gulf Stream transport like those observed. These are important to our upcoming study of low-frequency variability.

The time-mean total energy levels are compared for all 12 cases in Fig. 4.7, where total (horizontally and vertically integrated) energy is calculated as

$$E(t) = \frac{1}{HL_xL_y}\int\int_{\mathrm{D}_1}\left(\sum_{k=1}^{n}(1-l_k)\frac{(\nabla\psi_k)^2}{2} + \sum_{k=1}^{n-1}(1-l_{k+1})\frac{f_0^2(\psi_k-\psi_{k+1})^2}{2g'}\right)\mathrm{d}x\mathrm{d}y, \quad (4.3)$$

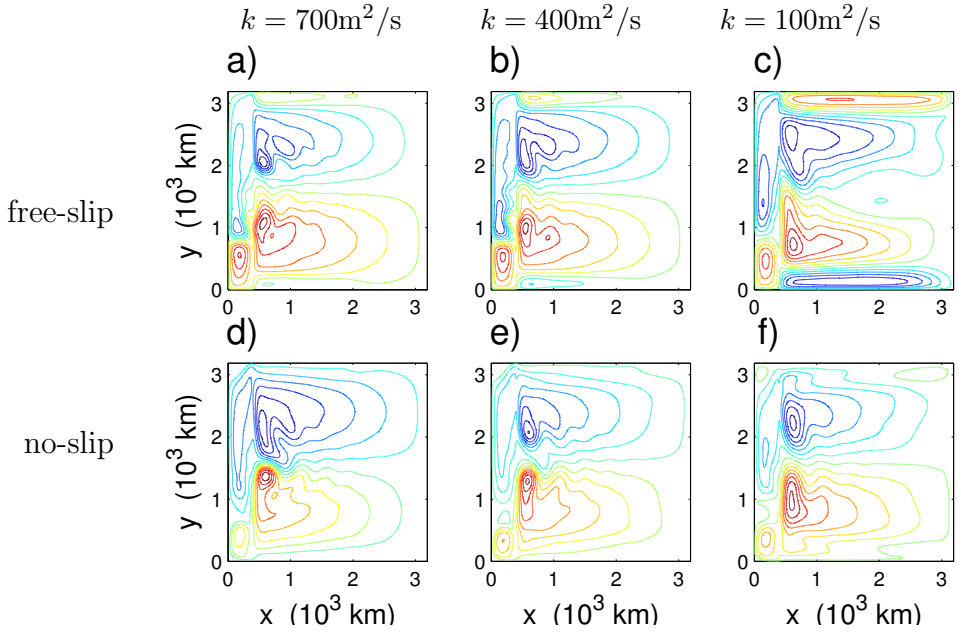


**Figure 4.2**. SHELF EXPERIMENTS: Time-mean barotropic streamfunction (C.I. = 10 Sv)

where $n = n(x, y)$ is the number of active layers. The levels in the Shelf experiments (for all parameter regimes) here also are comparable to the no-slip levels in the No-shelf experiments.

These results suggest, qualitatively and quantitatively, that a no-slip boundary in standard QG is a more accurate boundary compared to free-slip for oceans in the presence of shelves.

## 4.3 Time-mean circulation: dynamic comparison

In this section time-mean fields that describe eddy activity and mean circulation dynamics are examined. The time-mean eddy kinetic energy of the second layer in the Shelf experiments (Fig. 4.8) exhibits convergence to a distribution relatively insensitive to $\alpha$, as Re increases. (Note same area of the maxima in regimes c,f.) This is not the case in the No-shelf experiments (see Fig. 4.9): the distributions are quite different between free-slip and no-slip regimes, and the difference is as apparent in the high-Reynolds-number regimes (c,f) as in the low-Reynolds-number ones (a,d). The transition between the free-slip and

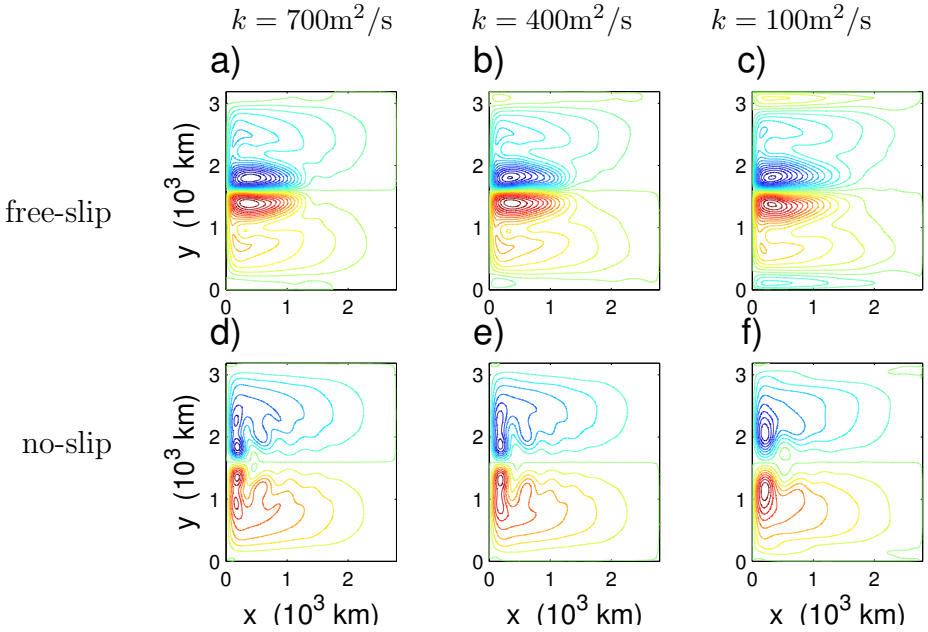


**Figure 4.3**. NO-SHELF EXPERIMENTS: Time-mean barotropic streamfunction (C.I. = 10 Sv)

no-slip regimes for the classical QG problem was examined by Haidvogel et al. [7] - see Fig 4.10, and we see the same dependence here in the no-shelf experiments.

Another important eddy-related variable is the eddy PV flux convergence. The time-averaged upper-layer QG equation is written as

$$J(\overline{\psi_1}, \overline{q_1}) = F_1 + \overline{\tilde{F}_1} + \overline{D_1}, \tag{4.4}$$

where $\overline{(\ )}$ and $(\ )'$ denote time-averaged and transient components, $F_1 = \frac{f_0}{H_1} w_e$ is the Ekman forcing, $\tilde{F}_1 = -J(\overline{\psi_1}, q_1') - J(\psi_1', \overline{q_1}) - J(\psi_1', q_1')$ is the eddy PV flux convergence, $\overline{D_1}$ is the time-mean dissipation due to lateral friction and (in the shelf case) bottom drag. $\tilde{F}_1$ is calculated from model results as

$$\tilde{F}_1 = J(\overline{\psi_1}, \overline{q_1}) - J(\psi_1, q_1).$$

Distributions of $\tilde{F}_1$ for the shelf experiment are shown in Fig. 4.11 (only the offshelf interior is shown). Local maxima are $\sim 10^{-11}$ s $^{-2}$ which is an order of magnitude bigger than the Ekman forcing amplitude. The difference between free-slip and no-slip cases becomes less apparent as Re increases (regimes c,f).

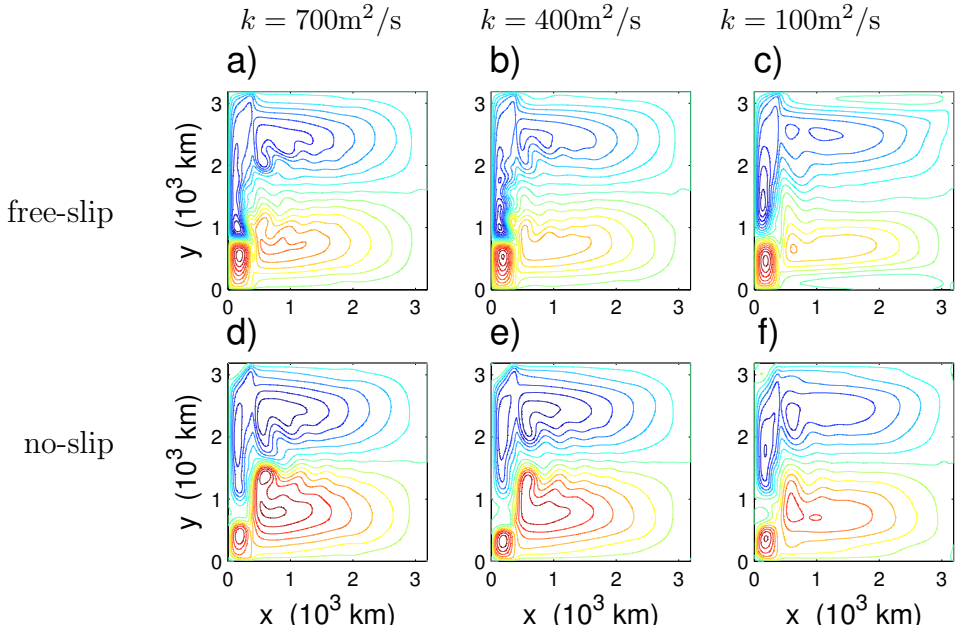


**Figure 4.4**. SHELF EXPERIMENTS: Time-mean 1st layer streamfunction (C.I. = 5 Sv)

Fig. 4.12 shows values of $\tilde{F}_1$ area-averaged over the subtropical and subpolar halves of the domain. The interpretation to be assigned to the numbers is that they represent the eddy PV fluxes into corresponding subdomains (normalized by their area). These consist of meridional eddy PV flux across the mid-latitude line and, for the Shelf experiments, the offshelf eddy PV fluxes. In the Shelf experiments (left panel) the North-South asymmetry created by the finite topography results in a net offshelf eddy PV flux which is the sum of the 'subtropical' and 'subpolar' values. As seen from Fig. 4.12, that total flux is positive, which is consistent with the results of study by Hallberg and Rhines [8], who showed that the areas of finite topography act as sources of positive PV for the interior. For comparison, the gyre-averaged Ekman forcing, $\frac{2}{\pi}\frac{f_0 w_0}{H_1}$, is $\approx 0.5 \times 10^{-12}$ s$^{-2}$ in comparison to which the eddy fluxes are $O(50\%)$.

Eddy PV flux convergence distributions in the No-shelf experiments are shown for comparison in Fig. 4.13. The difference between free-slip and no-slip regimes is persistent: In the free-slip regimes eddies and the meandering eastward jet balance the Ekman forcing by inter-gyre exchange of PV, whereas in the no-slip regimes almost no PV is exchanged

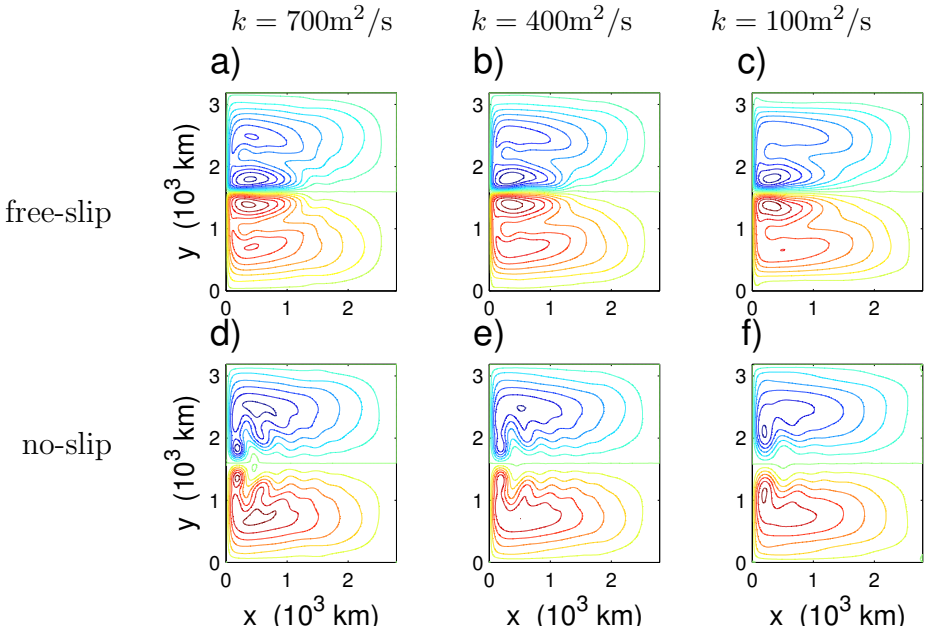


**Figure 4.5**. NO-SHELF EXPERIMENTS: Time-mean 1st layer streamfunction (C.I. = 5 Sv)

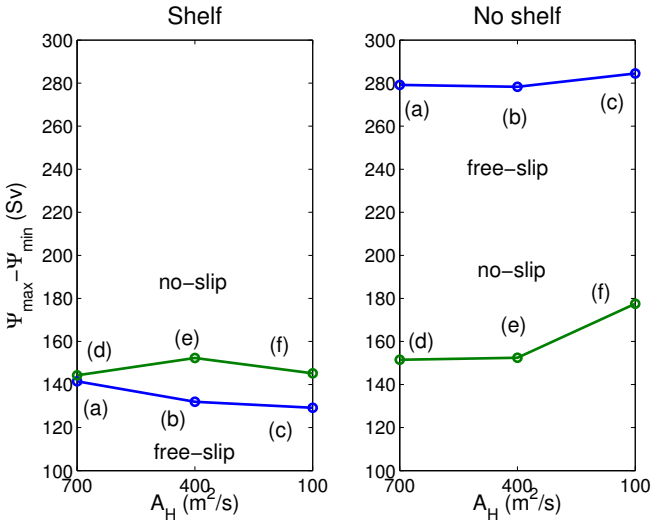


**Figure 4.6**. Net barotropic transport

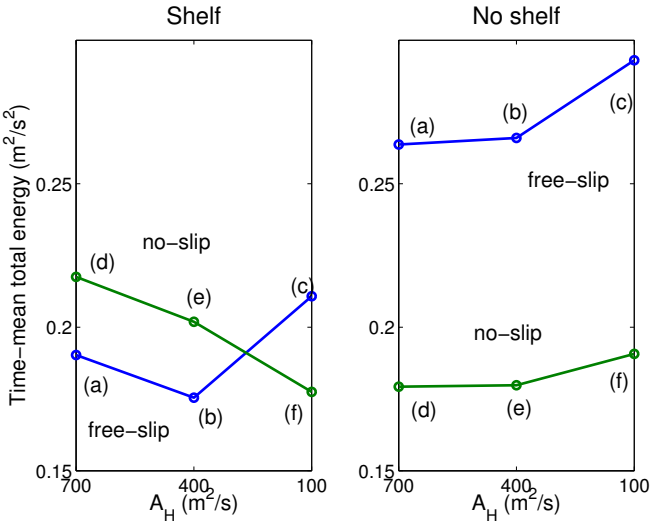


**Figure 4.7**. Time-mean total energy levels

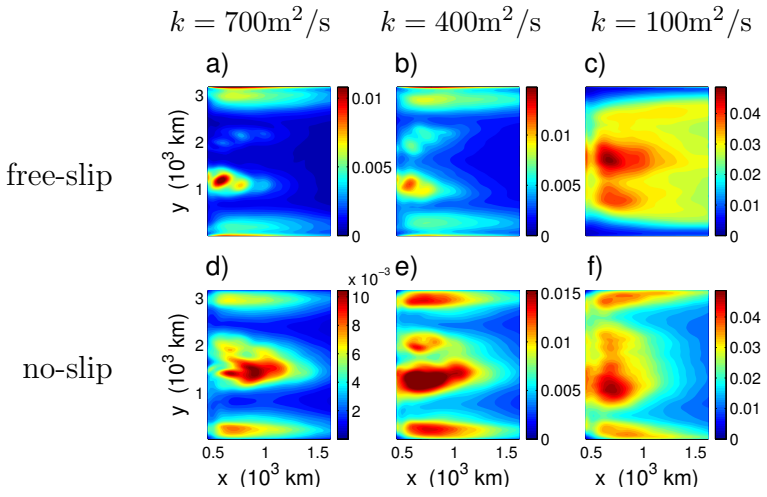


**Figure 4.8**. SHELF EXPERIMENTS: Time-mean 2nd layer eddy kinetic energy distributions, $m^2/s^2$ (the color scale changes from column to column and captures smaller of the two maxima in each column)

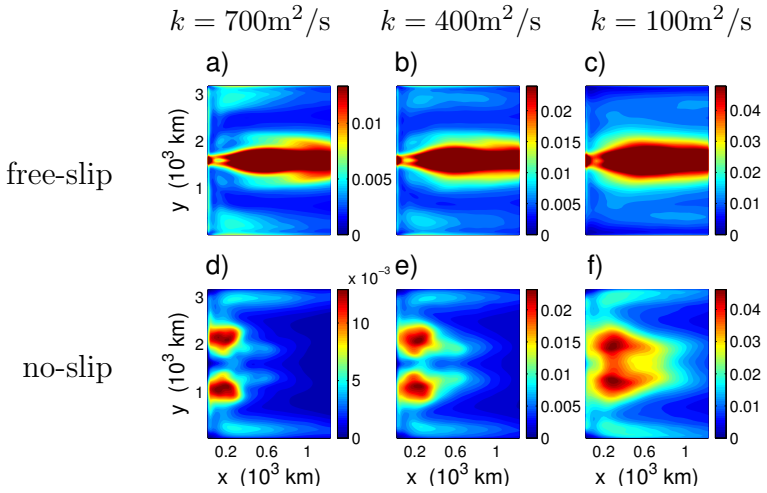


**Figure 4.9**. NO-SHELF EXPERIMENTS: Time-mean 2nd layer eddy kinetic energy distributions, $\mathrm{m}^2/\mathrm{s}^2$ (the color scale changes from column to column and captures smaller of the two maxima in each column)

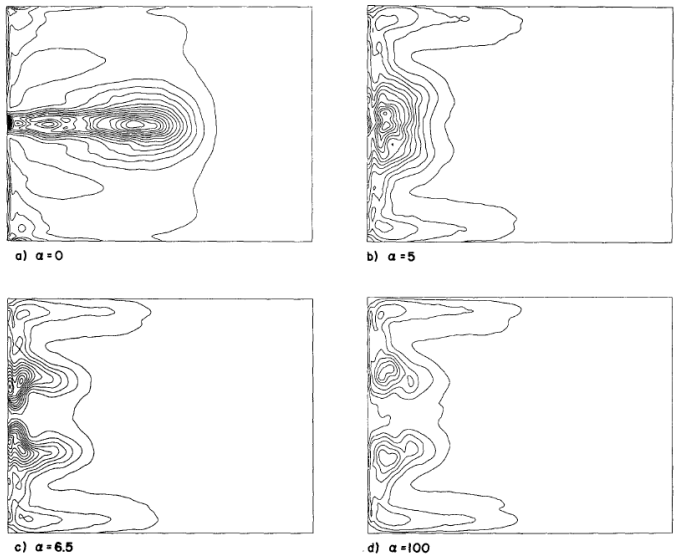


**Figure 4.10**. From Haidvogel et al., 1992: Time-mean 2nd layer eddy kinetic energy distributions in the 3-layer QG model for $\alpha = 0$ (free-slip) to 1 km $^{-1}$ (almost no-slip)

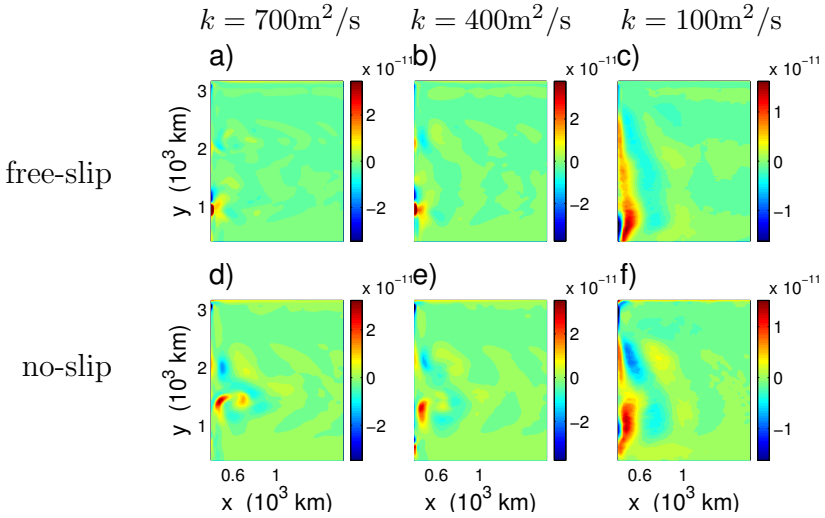


**Figure 4.11**. SHELF EXPERIMENTS: Time-mean upper layer eddy PV flux convergence in the offshelf interior, $\mathrm{s}^{-2}$ (western part is shown)

between gyres, and the western boundary is the dominant sink. No pronounced eastward jet is present - like in the Shelf experiments. That explains the difference in the meridional eddy PV flux between free-slip and no-slip regimes seen in Fig. 4.12 (right panel). This makes the shelf model similar to the no-slip regime of the standard QG model where the western boundary plays the role of finite topography, though the standard model does not provide the north-south asymmetry.

## 4.4 Analysis of variability

The time-mean fields examined in the previous sections show reduced sensitivity to $\alpha$ in the Shelf experiments compared to the standard QG results. The time-mean properties of the eddy fields show important contributions of the eddies to the time-mean flow. It is also thought that eddies can control intrinsic variability and define its spatial and temporal character. The 80 years of model output allows, at least qualitatively, to examine spatiotemporal patterns of variability, and check the hypothesis that they as well will be relatively insensitive to $\alpha$ in the Shelf experiments. For this purpose upper layer stream

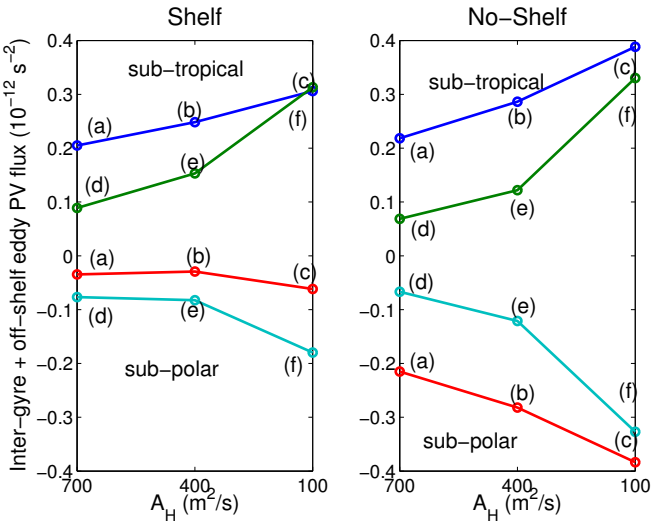


**Figure 4.12**. SHELF EXPERIMENTS: Time-mean offshelf eddy PV flux (normalized by area of the offshelf interior)

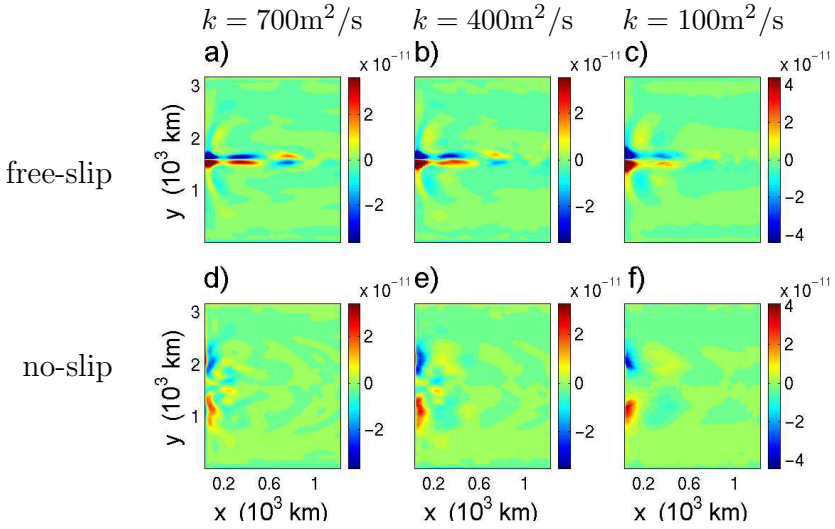


**Figure 4.13**. NO-SHELF EXPERIMENTS: Time-mean upper layer eddy PV flux convergence, s$^{-2}$ (western part of the domain is shown)

function is analyzed in this section using time filtering and EOF decomposition. This follows the approach adopted by Berloff and McWilliams in [2].

EOF decomposition [26] is performed on data anomalies (data with the time-mean spatial distribution subtracted out). Let an $N \times M$ matrix $F = \{f_{nm}\}$ represent the data anomalies ($n = 1, ..N,\ m = 1, ..M$), where $N$ is the number of spatial locations and $M$ is the number of observations at different times. EOF's (empirical orthogonal functions) are defined as the normalized orthogonal eigenvectors $E^{(k)} = \{e_{nk}\}$ of the covariance matrix $C$, estimated here as $C = \frac{1}{M} F F^T$, which is a symmetric matrix. As known from linear algebra,

$$CE = E\Lambda, \quad \Lambda = \mathrm{diag}\{\lambda_1, ..\lambda_N\}, \quad E^T E = I,$$

where $E = \{E^{(1)}, ...E^{(N)}\} = \{e_{nk}\}$ is the orthogonal matrix of eigenvectors, $I$ is the $N \times N$ unit matrix, and $\lambda_k$ are the eigenvalues, which add up to the total variance of the data, $\sigma^2 = \frac{1}{M} \sum f_{nm}^2$. The EOF's are usually ordered in decreasing eigenvalues: $\lambda_1 \geq \lambda_2 \geq ...\lambda_N \geq 0$. The matrix of data anomalies is thus decomposed as

$$F = EA = \sum_{k=1}^{N} E^{(k)} A_{(k)},$$

where $A = E^T F$ is the matrix whose rows $A_{(k)}$ are called the principal components (PC's). In our case, $M < N$, and the EOF's $E^{(k)}$ are calculated from the eigenvectors $\tilde{E}^{(k)}$ of the $M \times M$ matrix $\tilde{C} = \frac{1}{M} F^T F$:

$$E^{(k)} = F\tilde{E}^{(k)} / \sqrt{\lambda_k},\ k = 1, ..M$$

(note that the positive eigenvalues of $\tilde{C}$ and $C$ coincide, and for $M < N$ all eigenvalues of $\tilde{C}$ are positive). The EOF's are usually interpreted as dominant spatiotemporal patterns of variability. Their dynamical significance requires that they be connected to physical processes.

In the shelf experiment we focus on a box in the offshelf part of the domain, away from the zonal boundaries (where strong recirculations are present in the free-slip regimes): 20% of the meridional extent on each side is removed together with the shelf part. In the No-shelf experiments a box of the same size is taken. In both experiments the upper layer stream function output extracted from the box is low-pass time-filtered with a cutoff frequency of

0.58 $\text{yr}^{-1}$ (as was done by Berloff and McWilliams [2]). EOF decomposition of the filtered data is then performed.

The first three EOF's and corresponding principal components for the highest Reynolds number regimes (c) and (f) of the Shelf experiments are shown in Figure 4.14. The free-slip (c) regime first EOF with its zonally elongated structure does not have an analog in the no-slip regime (f). (In an experiment with free zonal boundaries one would anticipate that such a mode of variability would be absent in both free-slip and no-slip regimes.) However second and third EOF's in the free-slip (c) regime have structure similar to the first and second EOF's in the no-slip (f) regime. Their corresponding principal components also look qualitatively similar: for the given length of integration (80 yr) and frequency window (0-0.58 $\text{yr}^{-1}$) they have nearly flat spectra (see Figs. 4.16, 4.17). These pairs of EOF's thus represent spatiotemporal patterns of variability that are robust over different values of $\alpha$. The difference in fractional variances between corresponding PC's in the free-slip and no-slip cases can be attributed to the difference in total variance (note that the absolute values of the PC's are comparable). The total variances are expected to be different if the other parameters are kept same: in general, in the free-slip regime lateral friction is less efficient at dissipating energy than in the no-slip regime. The extra variance in the free-slip regime is found in the leading mode of large-scale variability (EOF 1) which is absent in the no-slip regime.

Figure 4.15 shows the EOF's and PC's for regimes (c) and (f) in the No-shelf experiments. Note that the first three EOF's explain a bigger portion of total variance than for the Shelf experiments. This may be attributed to the asymmetry introduced by the shelf: in the Shelf experiments the Ekman forcing is asymmetric with respect to the time-mean flow. In the No-shelf experiments, the low frequency variability patterns are distinct for the free-slip and no-slip regimes. In comparison, the first two EOF's in the no-slip regime (f) are qualitatively similar to the common pattern in the Shelf experiments. They are also consistent with the results of Berloff and McWilliams [2]: their second EOF of the low-pass filtered 2-layer solution with asymmetric Ekman forcing had a similar spatial structure, which was attributed to strengthening and weakening of the eastward jet and the associated countercurrents. These comparisons support the idea of using no-slip boundary conditions in the standard QG as a qualitatively accurate representation of shelf topography.

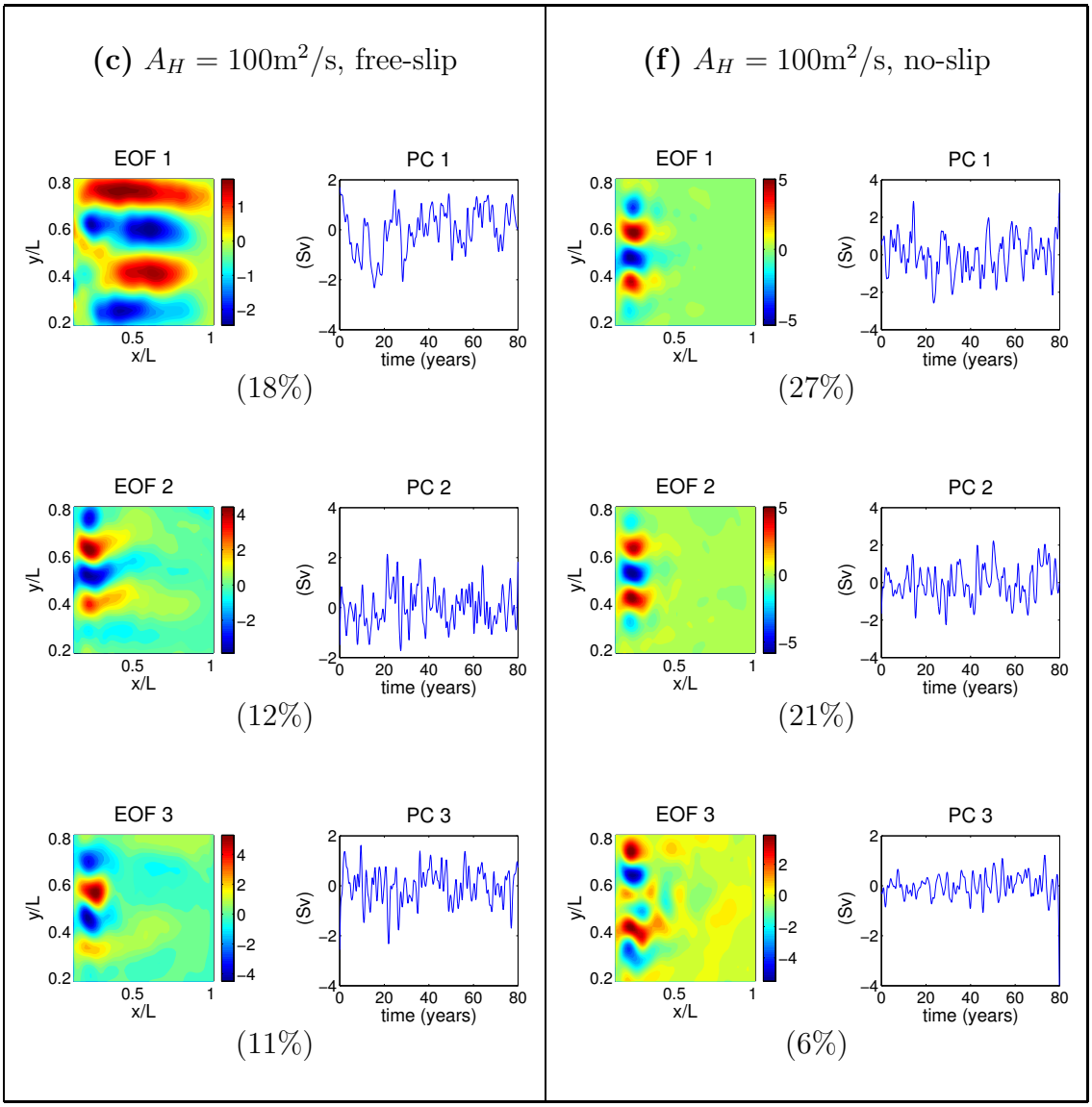


**Figure 4.14**. SHELF EXPERIMENTS: EOF decomposition of the offshelf upper layer stream function for regimes c and f. Fractional variance explained by each EOF is shown.

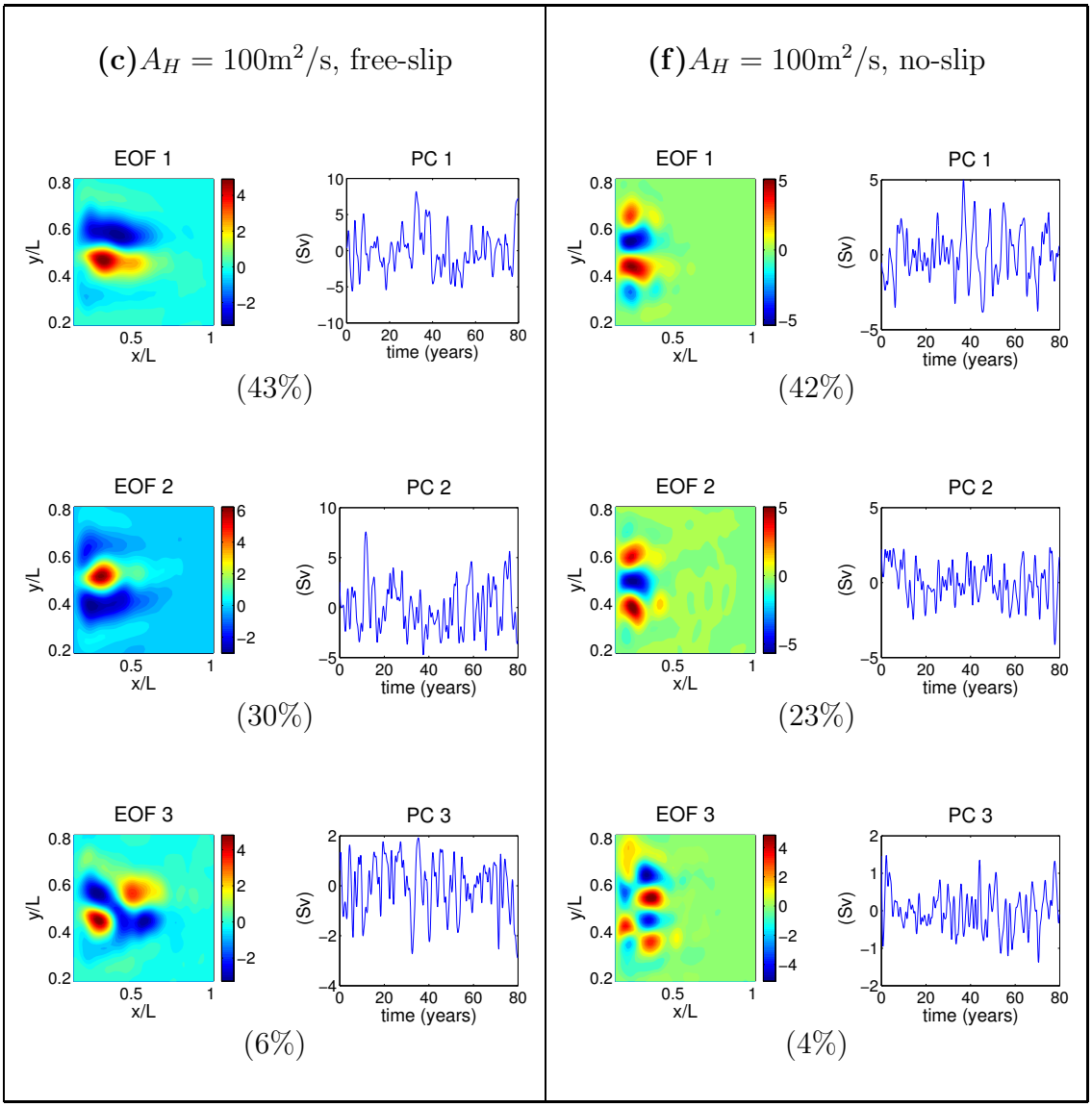


**Figure 4.15**. NO-SHELF EXPERIMENTS: EOF decomposition of the upper layer stream function for regimes c and f. Fractional variance explained by each EOF is shown.

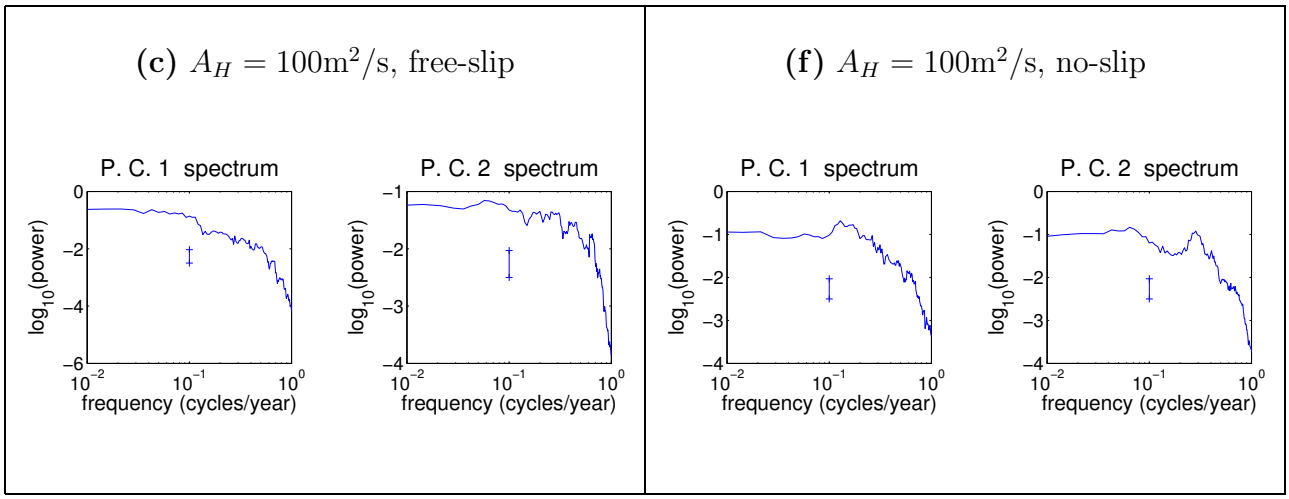


**Figure 4.16**. SHELF EXPERIMENTS: PC spectra of the offshelf upper layer stream function for regimes c and f. 80 % confidence intervals are shown.

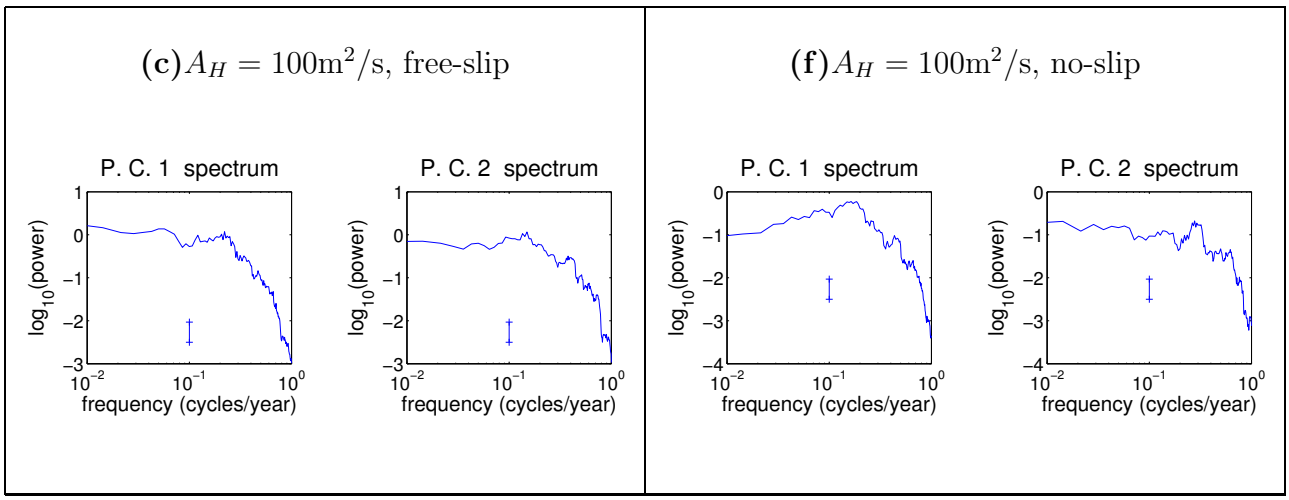


**Figure 4.17**. NO-SHELF EXPERIMENTS: PC spectra of the upper layer stream function for regimes c and f. 80 % confidence intervals are shown.

# CHAPTER 5

# CONCLUDING REMARKS

Finite amplitude topography has been taken into account within the framework of QG modeling. Using this modified approach, two aspects of the influence of finite amplitude topography on ocean variability have been examined. Topographic waves over finite amplitude abrupt topography have been addressed analytically and numerically. The wind-driven circulation has been examined in the presence of continental shelf topography.

## 5.1 Waves over finite topography

A weakly-nonlinear theory originally developed by Dewar and Leonov [6] has been applied here to weak disturbances over finite amplitude abrupt topography. In [6] the analysis was first applied to the case of weak topography (order Rossby number topographic variations within the lower layer). The linear results agreed with the previous studies by Rhines [29], [30], and Pratt and Stern [25]. The finite topography case was then considered. In the finite topography problem, the main linear result was that barotropic dynamics were filtered out. That result was consistent with the observed [24] pseudo-westward propagation of energy for all wavelengths in sinuous as well as varicose topographic modes.

The weakly-nonlinear theory has been extended here to include a term neglected in Dewar and Leonov [6]. The results have been tested against 2D numerical calculations by the modified QG model. The analytical/numerical agreement simultaneously justifies the extended theory and verifies the new numerical procedure. The interesting aspects to emerge from the weakly nonlinear theory are that the waves should break backward (pseudo-eastward) and that the steepening is stronger for offshelf disturbances. Both are verified by numerical experimentation.

Steep localized disturbances have been addressed numerically by the modified QG model. The asymmetry with respect to the sign of initial disturbance, noted in the weakly-nonlinear

regime, is especially pronounced for the overturning disturbances. It manifests in different mechanisms of wave braking: an onshelf initial disturbance results in a filamentation of the onshelf fluid into the offshelf regime, whereas an offshelf disturbance produces anticyclones which detach and transport offshelf fluid onto the shelf.

Thus, while onshelf water is quickly and efficiently mixed into the offshelf water very near to the topography, nearly pristine offshelf water can be expected to invade the shallow shelves. The dynamics and flows on the shelf can be expected to move the water to locations distinct from its origin. For example, in places where the onshelf direction is westward (as it is near the ocean western boundaries), the anticyclones will be carried onto the shelf by the beta effect.

Thus the onshelf−offshelf asymmetry in the wave breaking may result in a preferred onshelf transport of undiluted properties. Sea surface temperature (SST) exhibits sharp gradients in the western North Atlantic: the Mid-Atlantic Bight area was shown in [6] as an example where wavelike disturbances were clearly seen [24]. Further analysis of SST data is needed to check if there are manifestations of the asymmetry in the wave breaking and preferred onshelf transport mechanism predicted by this study.

## 5.2 Wind-driven circulation

QG numerical simulations of the wind-driven circulation with and without shelf topography have been conducted. Time-mean circulation and eddy fields in the Shelf experiment have shown reduced sensitivity to the type of boundary condition, especially at higher Reynolds numbers (Re), which was established by visual comparison of the time-mean fields and quantitative comparison of total levels of barotropic transport, energy and the offshelf eddy PV flux. The total time-mean levels of the offshelf eddy PV flux were positive, consistent with the study by Hallberg and Rhines [8].

Spatiotemporal patterns of intrinsic low-frequency variability common to the free-slip and no-slip regimes have been found in the Shelf experiment. All results of the Shelf experiment have been compared to corresponding results of the No-shelf (standard QG) experiments in the same parameter regimes. A basic conclusion from those comparisons is the overall resemblance of the shelf results to the no-slip standard QG results. Thus, the analysis

presented here adds some new physical foundation to the no-slip boundary conditions widely used in idealized modeling studies.

The robust patterns of low-frequency variability found in the Shelf experiments were also consistent with the results obtained by Berloff and McWilliams [2]. To make the comparison against [2] more complete, the onset of variability from smaller Re regimes needs to be considered.

Another important study where a standard QG model with no-slip boundary conditions was used, is the recent work by Siegel et al. [31], 2001, where the eddy variability in the wind-driven ocean circulation at very high resolution and Re was examined. Five basin-scale simulations were performed with horizontal resolution increasing up to 1.56 km and lateral friction decreasing down to 6.25 $m^2/s$. The interior-based Reynolds numbers seemed unusually small due to weak Ekman forcing: from 0.375 to 96, which was smaller than in our experiments. It should be noted however, that in our experiments, due to strong bottom drag, the eastward jet is not as sharply pronounced (especially in the Shelf experiments), and the actual locally-based Reynolds numbers are not as significantly increased compared to the interior-based Re.

Fig. 5.1 shows plots from Siegel et al. [31] of the upper layer PV anomaly in their five experiments with increasing horizontal resolution and Re. Coherent vortices appear and fill up the domain as Re increases (plots D and E), a situation qualitatively similar to the observed oceanic mesoscale structures. Levels of the eddy kinetic energy and eddy PV fluxes were measured in the experiments. Their growth with Re slowed down as the highest-Re regimes were reached. That indicated the possible existence of a saturated regime in the model at even higher Re where the eddy variability becomes roughly independent of Re.

It would be a critical extension of these results to attempt to drive the model described here into the coherent vortex regime. That should be possible given the support contained herein for the no-slip boundary conditions. The impacts on these solutions of the inherent topographically forced asymmetry and the explicit presence of the shelf, however, remain unknown.

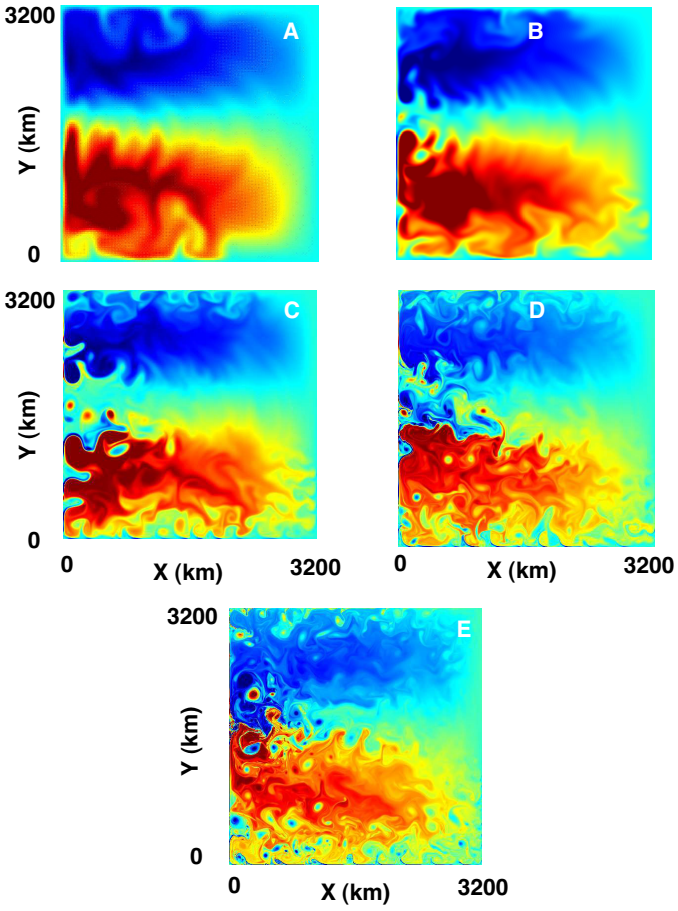


**Figure 5.1**. From Siegel et al.: snapshots of upper layer PV anomaly in experiments with horizontal resolution from 25 km (A) to 1.56 km (E)

# APPENDIX A

# INVERTING P.V. IN IRREGULAR DOMAINS WITH SHELVES: MODIFIED CAPACITANCE MATRIX METHOD

Cummins and Mysak [4] used the so-called Capacitance Matrix method to invert quasigeostrophic potential vorticity (PV) in domains with irregular lateral boundaries. (See also [28].) The irregular domain was augmented to a rectangular domain where a fast elliptic solver could be used. Artificial sources of PV were placed along the irregular boundary. The sources amplitudes were found from satisfying the no-normal flow boundary condition at the irregular boundary.

Using the same basic idea, we extend the numerical technique implemented in this thesis to more general geometry, including irregular topographic breaks.

The elliptic problem of inverting potential vorticity anomalies $\tilde{\mathbf{q}}$ into streamfunctions $\Psi$, after finite-volume discretization, is written

$$(\nabla_2^2 - \overline{A})\Psi = \tilde{\mathbf{q}}, \quad \Psi = \Psi^{(b)} \text{ at the boundaries,} \tag{A.1}$$

where

$$\nabla_2^2\psi(x_n, y_j) = \frac{\psi(x_{n+1}, y_j) + \psi(x_{n-1}, y_j) + \psi(x_n, y_{j+1}) + \psi(x_n, y_{j-1}) - 4\psi(x_n, y_j)}{\Delta x^2},$$

and matrix $\overline{A}$ is obtained from $A$, given given by (2.16), by area-averaging over neighboring grid cells. PV anomalies $\tilde{\mathbf{q}}$ are defined in (2.14), $\Psi^{(b)}$ is the vector of boundary values of the streamfunction. (In practice (2.15), (2.18) are solved, which are both of the form (A.1)).

In the areas of constant $n$ away from the topographic edges, $\overline{A} = A^{(n)} = \text{const}$, given by (2.16) for $n$ active layers. $A^{(n)}$, treated as an $n \times n$ matrix, may be diagonalized in the normal way:

$$A^{(n)} = T^{(n)}\Lambda^{(n)}T^{(n)^{-1}},$$

and the uncoupled equations for vertical modes $\Phi = {T^{(n)}}^{-1}\Psi$ can be written:

$$\nabla^2\Phi - \Lambda^{(n)}\Phi = {T^{(n)}}^{-1}\tilde{\mathbf{q}}, \tag{A.2}$$

where $\Lambda^{(n)} = \mathrm{diag}(\lambda_1^{(n)}, \ldots, \lambda_n^{(n)}) = \mathrm{diag}(0, {R_1^{(n)}}^{-2}, \ldots, {R_{n-1}^{(n)}}^{-2})$ is the matrix of eigenvalues of $A^{(n)}$, $R_k^{(n)}$ are the deformation radii, and $T^{(n)}$ is the transformation matrix consisting of the eigenvectors (vertical modes). In practice, $A^{(n)}$ is first made symmetric by a simple rescaling of variables, and then diagonalized. Thus, dropping the superscript $^{(n)}$, $T$ is found in the form $T = D^{-1}Q$, where $D$ is a diagonal matrix such that $DAD^{-1}$ is symmetric (we used $D = H^{-1/2}\mathrm{diag}(H_1^{1/2}, \ldots, H_n^{1/2})$, where $H = H_1 + \ldots + H_n$) and $Q$ is an orthogonal matrix of eigenvectors of $DAD^{-1}$.

$A$ will differ from (2.16) only at the edge grid nodes, where the number of active layers changes from $n$ to $m > n$ and the value of the function $l_n(x, y)$ jumps from 1 to 0.

The horizontal discretization chosen allows us to use a fast Helmholtz solver in a rectangular domain of a convenient size (FACR method: [9],[33]). The first step is to find, by solving (A.2), 'partial' solutions that satisfy (A.1) within interiors where $n$ is constant, then the solution is matched at the topographic breaks.

To illustrate, we consider a single-shelf case, and assume that the horizontal domain $\mathbf{D}$ is rectangular. The basin interior consists of an $n$-layer part $\mathbf{D}^{(\mathrm{I})}$ with a shelf at the bottom of the $n^{\mathrm{th}}$ layer ($n < N$), an $N$-layer part $\mathbf{D}^{(\mathrm{II})}$ and a shelf break $\mathbf{\Gamma}$ (see Fig. A.1):

$$\mathbf{D} = \mathbf{D}^{(\mathrm{I})} + \mathbf{D}^{(\mathrm{II})} + \mathbf{\Gamma} + \mathbf{B}, \tag{A.3}$$

where $\mathbf{B}$ is a rectangular boundary.

(A.1) can be written separately for $\mathbf{D}^{(\mathrm{I})},\ \mathbf{D}^{(\mathrm{II})},\ \mathbf{\Gamma},$ and $\mathbf{B}$:

$$(\nabla_2^2 - A^{(n)})[\Psi^{(\mathrm{I})}] = \mathbf{q}^{(\mathrm{I})}, \tag{A.4}$$

$$(\nabla_2^2 - A^{(N)})[\Psi^{(\mathrm{II})}] = \mathbf{q}^{(\mathrm{II})}, \tag{A.5}$$

$$(\nabla_2^2 - \overline{A})[\Psi^{(\Gamma)}] = \mathbf{q}^{(\Gamma)}, \tag{A.6}$$

$$\Psi(\mathbf{B}) = \Psi^{(b)\mathrm{B}}, \tag{A.7}$$

$$\begin{pmatrix} \psi_{n+1} \\ \vdots \\ \psi_N \end{pmatrix}(\mathbf{\Gamma}) = \begin{pmatrix} \psi_{n+1}^{(b)\Gamma} \\ \vdots \\ \psi_N^{(b)\Gamma} \end{pmatrix}, \tag{A.8}$$

where we have dropped the ˜ sign.

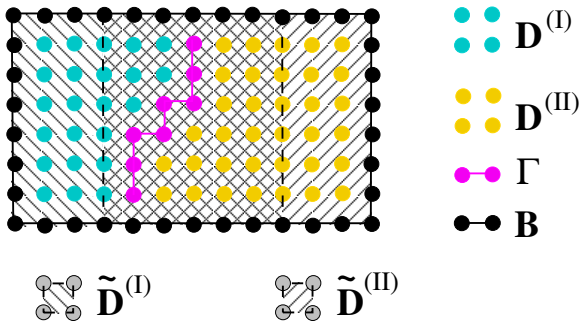


**Figure A.1**. Decomposition of horizontal grid: $n$-layer interior $\mathrm{D}^{(I)}$, $N$-layer interior $\mathrm{D}^{(II)}$, topographic break $\mathbf{\Gamma}$, regular outer boundary $\mathbf{B}$. Shaded are overlapping domains $\tilde{\mathbf{D}}^{(\mathrm{I})}$ and $\tilde{\mathbf{D}}^{(\mathrm{II})}$ where the fast solver is applied

(A.4) and (A.5) are diagonalized as it is usually done:

$$(\nabla_2^2 - \Lambda^{(n)})[\Phi^{(\mathrm{I})}] = {T^{(n)}}^{-1}\mathbf{q}^{(\mathrm{I})}, \quad \Psi^{(I)} = T^{(n)}\Phi^{(\mathrm{I})},$$

$$(\nabla_2^2 - \Lambda^{(N)})[\Phi^{(\mathrm{II})}] = {T^{(N)}}^{-1}\mathbf{q}^{(\mathrm{II})}, \quad \Psi^{(II)} = T^{(N)}\Phi^{(\mathrm{II})}$$

The subdomains $\mathbf{D}^{(\mathrm{I})}$ and $\mathbf{D}^{(\mathrm{II})}$ with their boundaries (each consisting of $\mathbf{\Gamma}$ and a part of $\mathbf{B}$) are augmented to corresponding rectangular domains $\tilde{\mathbf{D}}^{(\mathrm{I})}$ and $\tilde{\mathbf{D}}^{(\mathrm{II})}$ of optimal sizes (suitable for the fast Helmholtz solver) - see Fig. A.1. (A.4) and (A.5) are solved in $\tilde{\mathbf{D}}^{(\mathrm{I})}$ and $\tilde{\mathbf{D}}^{(\mathrm{II})}$ respectively subject to homogeneous boundary conditions by using the fast solver, the right-hand sides are set to zeroes in the augmented parts of the domains. As a result, 'partial' solutions $\Psi^{(\mathrm{Ip})}$ and $\Psi^{(\mathrm{IIp})}$ are obtained.

To satisfy (A.6) and (A.8), corrections are added to the partial solutions:

$$\Psi^{(\mathrm{I})} = \Psi^{(\mathrm{Ip})} + \Psi^{(\mathrm{Ic})}, \qquad \Psi^{(\mathrm{II})} = \Psi^{(\mathrm{IIp})} + \Psi^{(\mathrm{IIca})} + \Psi^{(\mathrm{IIcb})}, \tag{A.9}$$

where corrections $\Psi^{(\mathrm{Ic})}$, $\Psi^{(\mathrm{IIca})}$, $\Psi^{(\mathrm{IIcb})}$ can be formally written as:

$$\psi_k^{(\mathrm{Ic})}(\mathbf{x}) = \sum_{l=1}^{n}\sum_{\mathbf{x}'\in\Gamma}\xi_{l,\mathbf{x}'}\tilde{G}^{(\mathrm{I})}_{(l,k)}(\mathbf{x}',\mathbf{x}), \quad \psi_k^{(\mathrm{IIca})}(\mathbf{x}) = \sum_{l=1}^{n}\sum_{\mathbf{x}'\in\Gamma}\eta_{l,\mathbf{x}'}\tilde{G}^{(\mathrm{II})}_{(l,k)}(\mathbf{x}',\mathbf{x}), \tag{A.10}$$

$$\psi_k^{(\mathrm{IIcb})}(\mathbf{x}) = \sum_{l=n+1}^{N}\psi_l^{(b)\Gamma}\sum_{\mathbf{x}'\in\Gamma}\tilde{G}^{(\mathrm{II})}_{(l,k)}(\mathbf{x}',\mathbf{x}), \tag{A.11}$$

In (A.10-11) $\mathbf{x} = (x_i, y_j)$, $\mathbf{x}' = (x_{i'}, y_{j'})$ are grid nodes, and $\tilde{G}^{(\mathrm{I})}$ and $\tilde{G}^{(\mathrm{II})}$ are 'modified' Green's functions, i.e. homogeneous solutions with delta functions in the boundary conditions at $\Gamma$:

$$(\nabla_2^2 - A^{(n)})[\tilde{G}^{(\mathrm{I})}_{(l,k)}(\mathbf{x}', \mathbf{x})] = 0 \ \text{ in } \tilde{\mathbf{D}}^{(\mathrm{I})} \backslash \Gamma, \quad \tilde{G}^{(\mathrm{I})}_{(l,k)}(\mathbf{x}', \mathbf{x}) = \delta_{l,k}\delta_{\mathbf{x},\mathbf{x}'} \quad \text{for } \mathbf{x}, \mathbf{x}' \in \Gamma \tag{A.12}$$

$$(\nabla_2^2 - A^{(N)})[\tilde{G}^{(\mathrm{II})}_{(l,k)}(\mathbf{x}', \mathbf{x})] = 0 \ \text{ in } \tilde{\mathbf{D}}^{(\mathrm{II})} \backslash \Gamma, \quad \tilde{G}^{(\mathrm{II})}_{(l,k)}(\mathbf{x}', \mathbf{x}) = \delta_{l,k}\delta_{\mathbf{x},\mathbf{x}'} \quad \text{for } \mathbf{x}, \mathbf{x}' \in \Gamma \tag{A.13}$$

Both expressions in (A.9) should give the same result on $\Gamma$ in layers $1, \ldots, n$, so the weights $\xi$ and $\eta$ are not independent:

$$\xi_{l,\mathbf{x}'} + \psi_l^{(\mathrm{I})\mathrm{p}}(\mathbf{x}') \ = \ \eta_{l,\mathbf{x}'} + \psi_l^{(\mathrm{II})\mathrm{p}}(\mathbf{x}') \ = \ \psi_l(\mathbf{x}') \ = \ \zeta_{l,\mathbf{x}'}. \tag{A.14}$$

By substituting $\Psi(\Gamma) = (\Psi^{(\mathrm{I})} + \Psi^{(\mathrm{II})})/2$, where $\Psi^{(\mathrm{I})}$, $\Psi^{(\mathrm{II})}$ are defined in (A.9)-(A.14), into (A.6), we form a linear system for $Mn$ unknowns $\zeta_{l,\mathbf{x}'}$ where $M$ is the size of $\Gamma$. The matrix of coefficients of that system involves explicitly calculated $\tilde{G}^{(\mathrm{I})}(\mathbf{x}', \mathbf{x})$ and $\tilde{G}^{(\mathrm{II})}(\mathbf{x}', \mathbf{x})$ for $x$ in the vicinity of $\Gamma$:

$$\sum_{l=1}^{n} \sum_{\mathbf{x}' \in \Gamma} \tilde{C}_{(k,l);(\mathbf{x},\mathbf{x}')} \ \zeta_{l,\mathbf{x}'} \ = \ q_{k,\mathbf{x}}^{(\Gamma)} \ - \ q_{k,\mathbf{x}}^{(\Gamma\mathrm{p})} \ - \ \sum_{l=n+1}^{N} \tilde{A}_{l,\mathbf{x}} \ \psi_l^{(b)\Gamma}, \tag{A.15}$$

where $q_k^{(\Gamma\mathrm{p})} = L^{(\Gamma)}[(\psi_k^{(\mathrm{p})})]$.

The corrections (A.10) and (A.11) can be written in the form

$$\psi_k^{(\mathrm{Ic})}(\mathbf{x}) = \sum_{m=1}^{n} T_{km}^{(n)} \sum_{\mathbf{x}' \in \Gamma} q_{m,\mathbf{x}'}^{(\mathrm{Ic})} G_m^{(\mathrm{I})}(\mathbf{x}', \mathbf{x}), \tag{A.16}$$

$$\psi_k^{(\mathrm{IIca})}(\mathbf{x}) + \psi_k^{(\mathrm{IIcb})}(\mathbf{x}) = \sum_{m=1}^{N} T_{km}^{(N)} \sum_{\mathbf{x}' \in \Gamma} q_{m,\mathbf{x}'}^{(\mathrm{IIc})} G_m^{(\mathrm{II})}(\mathbf{x}', \mathbf{x}), \tag{A.17}$$

where $G_m^{(\mathrm{I})}(\mathbf{x}', \mathbf{x})$ and $G_m^{(\mathrm{II})}(\mathbf{x}', \mathbf{x})$ are modal Green's functions in $\tilde{\mathbf{D}}^{(\mathrm{I})}$ and $\tilde{\mathbf{D}}^{(\mathrm{II})}$, defined as

$$(\nabla_2^2 - \lambda_m^{(n)})[G_m^{(\mathrm{I})}(\mathbf{x}', \mathbf{x})] = \delta(\mathbf{x}', \mathbf{x}),$$

$$(\nabla_2^2 - \lambda_m^{(N)})[G_m^{(\mathrm{II})}(\mathbf{x}', \mathbf{x})] = \delta(\mathbf{x}', \mathbf{x})$$

(A.16) and (A.17) in practice mean inversion of modal potential vorticity anomalies $q_m^{(\mathrm{Ic})}$, $q_m^{(\mathrm{IIc})}$ in $\tilde{\mathbf{D}}^{(\mathrm{I})}$, $\tilde{\mathbf{D}}^{(\mathrm{II})}$ rather than use of explicitly calculated Green's functions. The anomalies $q_{m,\mathbf{x}'}^{(\mathrm{Ic})}$, $q_{m,\mathbf{x}'}^{(\mathrm{IIc})}$ satisfy

$$\sum_{\mathbf{x}''\in\Gamma} G_{(m)}^{(\mathrm{I})}(\mathbf{x}',\mathbf{x}'')\; q_{m,\mathbf{x}''}^{(\mathrm{Ic})} = \sum_{l=1}^{n} \left(T^{(n)^{-1}}\right)_{ml} \psi_l^{(\mathrm{Ic})}(\mathbf{x}'), \tag{A.18}$$

$$\sum_{\mathbf{x}''\in\Gamma} G_{(m)}^{(\mathrm{II})}(\mathbf{x}',\mathbf{x}'')\; q_{m,\mathbf{x}''}^{(\mathrm{IIc})} = \sum_{l=1}^{n} \left(T^{(N)^{-1}}\right)_{ml} \psi_l^{(\mathrm{IIc})}(\mathbf{x}'), \tag{A.19}$$

where $\psi_l^{(\mathrm{IIc})} = \psi_l^{(\mathrm{IIca})} + \psi_l^{(\mathrm{IIcb})}$. The matrices in the left-hand sides of (A.18), (A.19) are called inverse capacitance matrices:

$$\left(C_{(m)}^{(\mathrm{I})^{-1}}\right)_{\mathbf{x}',\mathbf{x}''} = G_{(m)}^{(\mathrm{I})}(\mathbf{x}',\mathbf{x}''), \qquad \left(C_{(m)}^{(\mathrm{II})^{-1}}\right)_{\mathbf{x}',\mathbf{x}''} = G_{(m)}^{(\mathrm{II})}(\mathbf{x}',\mathbf{x}''). \tag{A.20}$$

In the pre-processing stage $C_{(m)}^{(\mathrm{I})^{-1}}$ and $C_{(m)}^{(\mathrm{II})^{-1}}$ are calculated. Then matrices $\tilde{C}$, $\tilde{A}$ in (A.15) are calculated which involves explicit calculation of $\tilde{G}_{(l,k)}^{(\mathrm{I})}(\mathbf{x}',\mathbf{x})$, $\tilde{G}_{(l,k)}^{(\mathrm{II})}(\mathbf{x}',\mathbf{x})$ defined in (A.12), (A.13) for grid points $\mathbf{x}$ neighboring $\Gamma$. That is done by solving the capacitance matrix problems (A.18), (A.19) with the right-hand sides known from the definition of $\tilde{G}^{(\mathrm{I})}$ and $\tilde{G}^{(\mathrm{II})}$, and inverting the obtained potential vorticity anomalies.

For a given right-hand side of (A.4) - (A.8), partial solutions $\Psi^{(\mathrm{Ip})}$, $\Psi^{(\mathrm{IIp})}$ are first obtained, and the next step is to solve (A.15). A direct solver with iterative correction can be used. Then the capacitance matrix problems (A.18) and (A.19) are solved directly and the corrections are calculated and added to the partial solutions. This procedure can be generalized to allow multiple shelf breaks.

# APPENDIX B

# DERIVATION OF WEAKLY-NONLINEAR FRONTAL EQUATION

## 1. Properties of Green functions

Barotropic and baroclinic Green functions $G_b$ and $G_c$ are defined by equations (3.6-7) subject to zero boundary conditions at infinity. The Fourier-transformed forms of (3.6-7) are

$$(-k^2 + \partial_y)\widehat{G_b}(k,y) = \delta(y), \qquad (-\kappa^2 + \partial_y)\widehat{G_c}(k,y) = \delta(y), \tag{B.1}$$

where

$$\kappa^2 = k^2 + R^{-2}, \tag{B.2}$$

and the Fourier transform $\widehat{(\ )}$ is defined as

$$\widehat{f}(k) = \int_{-\infty}^{\infty} f(x)e^{-ikx}\mathrm{d}x \tag{B.3}$$

The solutions of (B.1) that meet boundary conditions $\widehat{G_b}(\pm\infty) = 0$, $\widehat{G_c}(\pm\infty) = 0$ are

$$\widehat{G_b}(k,y) = -\frac{e^{-|ky|}}{2|k|}, \qquad \widehat{G_c}(k,y) = -\frac{e^{-|\kappa y|}}{2|\kappa|} \tag{B.4}$$

Below are their properties that will be important in what follows ($G$ will be used in statements that apply to both $G_b$ and $G_c$):

1.

$$\begin{aligned} \widehat{G}(k,-y) &= \widehat{G}(k,y), \\ \partial_y\widehat{G}(k,-y) &= -\partial_y\widehat{G}(k,y) \end{aligned} \tag{B.5}$$

2.

$$\int_0^a \widehat{G_b}(k,y)\mathrm{d}y = -\frac{1-e^{-|ka|}}{2k^2}\mathrm{sign}a, \qquad \int_0^a \widehat{G_c}(k,y)\mathrm{d}y = -\frac{1-e^{-|\kappa a|}}{2\kappa^2}\mathrm{sign}a \tag{B.6}$$

Let $\psi(x,y) = \int_{-\infty}^{\infty}\int_{0}^{L(\xi)} G(x-\xi, y-\eta)\mathrm{d}\eta\mathrm{d}\xi$. Then

3.

$$\widehat{\psi}(k,0) = \int_{-\infty}^{\infty}\left(\int_{0}^{L(\xi)} \widehat{G}(k,\eta)\mathrm{d}\eta\right) e^{-ik\xi}\mathrm{d}\xi; \tag{B.7}$$

4.

$$\widehat{\psi}_y(k,0) = -\int_{-\infty}^{\infty} \widehat{G}(k,\eta)\Big|_{0}^{L(\xi)} e^{-ik\xi}\mathrm{d}\xi. \tag{B.8}$$

Properties 3 and 4 follow from property 1:

$\widehat{\psi}(k,0) = \int_{-\infty}^{\infty}\left(\int_{-\infty}^{\infty}\int_{0}^{L(\xi)} G(x-\xi,\eta)\mathrm{d}\eta\mathrm{d}\xi\right)e^{-ikx}\mathrm{d}x =$
$\int_{-\infty}^{\infty}\int_{0}^{L(\xi)}\left(\int_{-\infty}^{\infty} G(x-\xi,\eta)e^{-ikx}\mathrm{d}x\right)\mathrm{d}\eta\mathrm{d}\xi = \int_{-\infty}^{\infty}\int_{0}^{L(\xi)}\left(\int_{-\infty}^{\infty} G(x',\eta)e^{-ikx'}\mathrm{d}x'\right)\mathrm{d}\eta e^{-ik\xi}\mathrm{d}\xi,$

$\widehat{\psi}_y(k,0) = \int_{-\infty}^{\infty}\left(\int_{-\infty}^{\infty}\int_{0}^{L(\xi)} G_y(x-\xi,y-\eta)|_{y=0}\mathrm{d}\eta\mathrm{d}\xi\right)e^{-ikx}\mathrm{d}x =$
$\int_{-\infty}^{\infty}\int_{0}^{L(\xi)}\left(-\int_{-\infty}^{\infty} G_\eta(x-\xi,\eta)e^{-ikx}\mathrm{d}x\right)\mathrm{d}\eta\mathrm{d}\xi = -\int_{-\infty}^{\infty}\int_{0}^{L(\xi)}\mathrm{d}\left(\int_{-\infty}^{\infty} G(x',\eta)e^{-ikx'}\mathrm{d}x'\right)e^{-ik\xi}\mathrm{d}\xi$

## 2. Fourier-transformed formal solution

Applying properties 3, 4, 2, and the expressions (B.4) to the formal solution (3.8) gives

$$\widehat{\psi_b}(k,0,t) = -\frac{\widehat{\theta_b}}{2|k|} - \frac{H_1}{H}\frac{q_0}{2|k|}I_k[L_-], \qquad \widehat{\psi_b}_y(k,0,t) = -\frac{\widehat{\theta_b}}{2} + \frac{H_1}{H}\frac{q_0}{2}I_k[L_-] \tag{B.9}$$

$$\widehat{\psi_c}(k,0,t) = -\frac{\widehat{\theta_c}}{2|\kappa|} - \frac{q_0}{2|\kappa|}I_\kappa[L_-], \qquad \widehat{\psi_c}_y(k,0,t) = -\frac{\widehat{\theta_c}}{2} + \frac{q_0}{2}I_\kappa[L_-] \tag{B.10}$$

$$\widehat{\psi_1}(k,0,t) = -\frac{\widehat{\theta_1}}{2|k|} + \frac{q_0}{2|k|}I_k[L_+], \qquad \widehat{\psi_1}_y(k,0,t) = \frac{\widehat{\theta_1}}{2} + \frac{q_0}{2}I_k[L_+] \tag{B.11}$$

where transforms $I_k$, $I_\kappa$ are defined as

$$I_k[f](k) = \int_{-\infty}^{\infty}\frac{1-e^{-|kf(x)|}}{|k|}e^{-ikx}\mathrm{d}x, \qquad I_\kappa[f](k) = \int_{-\infty}^{\infty}\frac{1-e^{-|\kappa f(x)|}}{|\kappa|}e^{-ikx}\mathrm{d}x \tag{B.12}$$

The boundary conditions (3.5) can be written as

$$\begin{array}{ll} \widehat{\psi_1} = & \widehat{\psi_c}, \\ H\widehat{\psi_b} = & H_1\widehat{\psi_c}, \\ H(\widehat{\psi_1}_y - \widehat{\psi_b}_y) = & H_2\widehat{\psi_c}_y \end{array} \tag{B.13}$$

Eliminating $\widehat{\theta_c}$ and $\widehat{\theta_b}$ gives

$$\widehat{\theta_1} = -q_0 \frac{(k-\kappa)H_2 I_k[L_+] - 2k(H_1 I_k + H_2 I_\kappa)[L_-]}{k(2H-H_2)+\kappa H_2}, \tag{B.14}$$

where $\kappa = \mathrm{sign}k\sqrt{k^2+R^{-2}}$.

In the small steepness regime $|kL| \le |\kappa L| \ll 1$ the nonlinear transforms $I_k$, $I_\kappa$ are approximated by the quadratic asymptotic formed by Taylor expansion

$$I_k[L_+] \approx \widehat{L_+} - \frac{|k|}{2}\widehat{L_+^2}, \qquad I_k[L_-] \approx -\widehat{L_-} - \frac{|k|}{2}\widehat{L_-^2},$$

$$I_\kappa[L_-] \approx -\widehat{L_-} - \frac{|\kappa|}{2}\widehat{L_-^2}.$$

Thus (B.11) can be approximated as:

$$\widehat{\psi_1}(k,0,t) = -\frac{\widehat{\theta}_{1(\mathrm{lin})}}{2|k|} + \frac{q_0}{2|k|}\widehat{L_+} \; - \; \frac{\widehat{\theta}_{1(\mathrm{quad})}}{2|k|} - \frac{q_0}{4}\widehat{L_+^2} \; + \; O(q_0 L^3), \tag{B.15}$$

$$\psi_{1y}(x,0,t) = \frac{\theta_{1(\mathrm{lin})}}{2} + \frac{q_0}{2}L_+ \; + \; O(q_0 k L^2), \tag{B.16}$$

where

$$\widehat{\theta}_{1(\mathrm{lin})} = q_0 \frac{(\kappa-k)H_2\widehat{L_+} - 2kH\widehat{L_-}}{k(2H-H_2)+\kappa H_2}, \tag{B.17}$$

$$\widehat{\theta}_{1(\mathrm{quad})} = -\frac{q_0|k|}{2}\frac{(\kappa-k)H_2\widehat{L_+^2} + 2(kH_1+\kappa H_2)\widehat{L_-^2}}{k(2H-H_2)+\kappa H_2} \tag{B.18}$$

From (B.15) $\psi_{1xx} = O(q_0 k L)$, and thus

$$\psi_{1yy}(x,0\pm,t) = -q_0 \mathrm{sign}L + O(q_0 k L) \tag{B.19}$$

Substituting (B.16) and (B.19) into the expansion (3.9) gives

$$\psi_{1L} \equiv \psi_1(x,L,t) = \psi_1(x,0,t) \; + \; \frac{\theta_{1(\mathrm{lin})}L}{2} \; + \; \frac{q_0}{2}L_-^2 \; + \; O(q_0 k L^3)$$

Using (B.15), (B.17), (B.18), we finally obtain:

$$\widehat{\psi_{1L}} = \widehat{\psi_{1L}}_{(\mathrm{lin})} + \widehat{\psi_{1L}}_{(\mathrm{quad})} + O(L^3), \quad \text{where}$$

$$\widehat{\psi_{1L}}_{(\mathrm{lin})} = \frac{q_0}{2|k|}\frac{2kH}{k(2H-H_2)+\kappa H_2}\widehat{L}, \tag{B.20}$$

$$\widehat{\psi_{1L}}_{(\mathrm{quad})} = \frac{\widehat{\theta_{1(\mathrm{lin})}}L}{2} - \frac{q_0}{2}\frac{kH\widehat{L_+^2} - [3kH + 2(\kappa-k)H_2]\,\widehat{L_-^2}}{k(2H-H_2)+\kappa H_2}, \tag{B.21}$$

which results in (3.10).

# REFERENCES


[1] Arakawa, A. Computational design for long-term numerical integration of the equations of fluid motion: two-dimensional incompressible flow. *J. Comp. Phys.*, 1:119–143, 1966.

[2] Berloff, P. S. and J. C. McWilliams. Large-scale, low-frequency variability in wind-driven ocean gyres. *J. Phys. Oceanogr.*, 27:1925–1949, 1999.

[3] Brachet, S., P. Y. Le Traon, and C. Le Provost. Mesoscale variability from a high-resolution model and from altimeter data in the North Atlantic Ocean. *J. Geophys. Res. - Oceans*, 109(C12), 2004.

[4] Cummins, P. and L. A. Mysak. A Quasi-geostrophic circulation model of the North East Pacific. Part I. A preliminary numerical experiment. *J. Phys. Oceanogr.*, 18:1261–1286, 1988.

[5] Dewar, W. K. Nonlinear midlatitude ocean adjustment. *J. Phys. Oceanogr.*, 33:1057–1082, 2003.

[6] Dewar, W. K. and D. Leonov. Variability on steep, confined topography. *Deep-Sea Res. II*, 51:2973–2993, 2004.

[7] Haidvogel, D. B., J. C. McWilliams, and P. Gent. Boundary current separation in a quasigeostrophic, eddy-resolving ocean circulation model. *J. Phys. Oceanogr.*, 22:882–902, 1992.

[8] Hallberg, R. and P. B. Rhines. Boundary sources of potential vorticity in geophysical circulations. In R. M. Kerr and Y. Kimura, editors, *Developments in Geophysical Turbulence*, pages 51–65. Kluwer, 2000.

[9] Hockney, R. W. A fast direct solution of Poissonś equation using Fourier analysis. *J. Assoc. Computing Machinery*, 12(1):95–113, 1965.

[10] Hogg, A.M., W. K. Dewar, P. Killworth, and J. Blundell. A quasi-geostrophic coupled model (Q-GCM). *Mon. Wea. Rev.*, 131(10):2261–2278, 2003.

[11] Hogg, N. G. On the transport of the Gulf Stream between Cape Hatteras and the Grand Banks. *Deep-Sea Res. A*, 39(7-8A):1231–1246, 1992.

[12] Holland, W. R. The role of mesoscale eddies in the general circulation of the ocean − numerical experiments using a wind-driven quasi-geostrophic model. *J. Phys. Oceanogr.*, 8:363–392, 1978.

[13] Hurrell, J. W. Decadal trends in the North-Atlantic Oscillation - regional temperatures and precipitation. *Science*, 269:676–679, 1995.

[14] Kravtsov, S. and A. Robertson. Midlatitude ocean-atmosphere interaction in an idealized coupled model. *Climate Dynamics*, 19(8):693–711, 2002.

[15] LaCasce, J. H. and J. Pedlosky. Baroclinic Rossby waves in irregular basins. *J. Phys. Oceanogr.*, 32, 2002.

[16] Lentz, S. J. and J. H. Trowbridge. The bottom boundary layer over the Northern California shelf. *J. Phys. Oceanogr.*, 21(8):1186–1201, 1991.

[17] MacCready, P. and P. B. Rhines. Buoyant inhibition of Ekman transport on a slope and its effect on stratified spin-up. *J. Fluid Mech.*, 223:631–661, 1991.

[18] Marshall, J., Y. Kushnir, D. Battisti, P. Chang, A. Czaja, R. Dickson, J. Hurrell, M. McCartney, R. Saravanan, and M. Visbeck. North Atlantic climate variability: Phenomena, impacts and mechanisms. *Int. J. of Climatology*, 21(15):1863–1898, 2001.

[19] McWilliams, J. C. A note on a consistent qasigeostrophic model in a multiply connected domain. *Dyn. Atmos. and Oceans*, 1:427–441, 1977.

[20] Mysak, L. A., E. Johnson, and W. Hsieh. Baroclinic and barotropic instabilities in coastal currents. *J. Phys. Oceanogr.*, 11(2):209–230, 1981.

[21] Pedlosky, J. *Geophysical Fluid Dynamics*. Springer-Verlag, 2$^{\text{nd}}$ edition, 1987.

[22] Pedlosky, J. The transmission and transformation of baroclinic Rossby waves by topography. *J. Phys. Oceanogr.*, 30, 2000.

[23] Penduff, T., B. Barnier, W. K. Dewar, and J. J. O'Brien. Dynamical response of the oceanic eddy field to the North Atlantic Oscillation: A model-data comparison. *J. Phys. Oceanogr.*, 34(12):2615–2629, 2004.

[24] Pickart, R. Gulf Stream-generated topographic Rossby waves. *J. Phys. Oceanogr.*, 25(4):514–586, 1995.

[25] Pratt, L. J. and M. E. Stern. Dynamics of potential vorticity fronts and eddy detachment. *J. Phys. Oceanogr.*, 1986.

[26] Preisendorfer, R. W. *Principal Component analysis in meteorology and oceanography.* Elsevier, New York, 1988.

[27] Primeau, F. W. Multiple equilibria of a double-gyre ocean model with super-slip boundary conditions. *J. Phys. Oceanogr.*, 28(11):2130–2147, 1998.

[28] Proskurowski, W. and O. Widlund. On the numerical solution of Helmholtzś equation by the Capacitance Matrix method. *Math. Comput.*, 30(135):433–468, 1976.

[29] Rhines, P. B. Slow oscillations in an ocean of varying depth. Part 1. Abrupt topography. *J. Fluid Mech.*, 37(1):161–189, 1969.

[30] Rhines, P. B. Edge-, bottom-, and Rossby waves in a rotating stratified fluid. *Geophysical Fluid dynamics*, 1:273–302, 1970.

[31] Siegel, A., J. Weiss, J. Toomre, J. C. McWilliams, P. S. Berloff, and I. Yavneh. Eddies and vortices in ocean basin dynamics. *Geophys. Res. Letters*, 28(16):3183–3186, 2001.

[32] Simonnet, E. and H. Dijkstra. Spontaneous generation of low-frequency modes of variability in the wind-driven ocean circulation. *J. Phys. Oceanogr.*, 32:1747–1762, 2002.

[33] Swarztrauber, P. N. Methods of cyclic reduction, Fourier-analysis and FACR algorithm for discrete solution of Poissons' equation on a rectangle. *SIAM Review*, 19(3):490–501, 1977.

[34] Thompson, L. Two-layer quasigeostrophic flow over finite isolated topography. *J. Phys. Oceanogr.*, 23:1297–1314, 1993.

[35] Volkov, D. L. and H. M. van Aken. Annual and interannual variability of sea level in the northern North Atlantic Ocean. *J. Geophys. Res. - Oceans*, 108(C6), 2003.

[36] Wunsch, C. The interpretation of short climate records, with comments on the North Atlantic and Southern Oscillations. *Bulletin Amer. Met. Soc.*, 80(2):245–255, 1999.

# BIOGRAPHICAL SKETCH

**Dmitri A. Leonov**

## EDUCATION

• 2005: **Ph.D.** Oceanography. Department of Oceanography, Florida State Univerlity, USA

• 1999: **M.S.** Physics. Faculty of Physics, Lomonosov Moscow State University, Russia

## RESEARCH EXPERIENCE

• 2001-2005: Graduate research assistant, Department of Oceanography, Florida State University. Designed and implemented a domain decomposition method for solving QG equations in presence of irregular steep topography. Supervisor: W. K. Dewar.

• 2000-2001: Graduate research assistant, Department of Oceanography, Florida State University. Worked under supervision of M. E. Stern and T. Radko on implementing 2D direct numerical simulations of salt-finger convection using Fourier spectral methods.

## PUBLICATIONS AND PRESENTATIONS

• Dewar, W. K. and D. A. Leonov, 2004: Variability on steep, confined topography. Deep Sea Res. II, 51: 2973-2993

• Dewar, W. K. and D. A. Leonov, 2004: Variability on steep, confined topography. 12th Ocean Sciences Meeting. Portland, Oregon. 26-30 January 2004 (poster)

## PERSONAL INFORMATION

• Married, one child